Experimental overview of Deeply Virtual Compton Scattering

N. D'hose, S. Niccolai, A. Rostomyan

Review

Experimental overview of Deeply Virtual Compton Scattering[⋆]

Nicole d'Hose[1], Silvia Niccolai[2,a], and Armine Rostomyan[3]

[1] CEA-Saclay, DRF/Irfu/SPhN, 91191 Gif-sur-Yvette, France
[2] Institut de Physique Nucléaire d'Orsay, Orsay, France
[3] DESY, 22603 Hamburg, Germany

Abstract. Deeply Virtual Compton Scattering (DVCS) is a key reaction to gain information on Generalized Parton Distributions. In this paper the existing measurements of DVCS on the nucleon, as well as those planned for the near future, are presented and discussed.
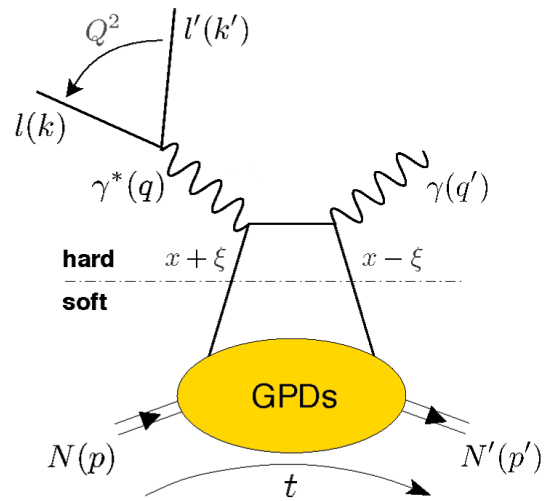
1 Introduction

Our understanding of nucleon structure has been improving recently thanks to the ongoing intense effort of research on Generalized Parton Distributions (GPDs). These structure functions describe the correlations between the longitudinal momentum and transverse spatial position of the partons inside the nucleon, and, among other features, they give access to the contribution of the orbital angular momentum of the quarks and gluons to the spin of the nucleon. They are also sensitive to the correlated quark-antiquark components in the nucleon. A general overview on GPDs and details on the formalism can be found in [1] (this issue) as well as in refs. [2–16].

The nucleon GPDs are accessible via measurements of hard exclusive leptoproduction of a real photon, $\ell N \to \ell' N' \gamma$ (where the $\gamma^* N \to N' \gamma$ subprocess is called deeply virtual Compton scattering, DVCS), or of a meson (deeply virtual meson production, DVMP, detailed in another paper of this Topical Issue [17]), as well as in time-like Compton scattering (TCS, $\gamma N \to N' \gamma^*$).

Figure 1 illustrates the leading process for DVCS, also called "handbag diagram". Here k and k' are the four momenta of the incoming (l) and scattered (l') leptons, respectively, and p and p' are the four momenta of the initial-(N) and final-state (N') nucleons. The virtual photon interacts with a quark in the nucleon having a longitudinal-momentum fraction $x + \xi$. The quark is then reabsorbed in the nucleon with a momentum fraction $x - \xi$, and a real photon is emitted.

Conditions are required for the applicability of the GPD formalism and the validity of the handbag approxi-

---

[⋆] Contribution to the Topical Issue "The 3-D Structure of the Nucleon" edited by Mauro Anselmino, Michel Guidal, Patrizia Rossi.
[a] e-mail: `silvia@jlab.org`

Fig. 1. The handbag diagram for the DVCS process on the nucleon $\ell N \to \ell' N' \gamma$. The four-momenta of the incoming and outgoing leptons are labeled as, respectively, k and k', while those of the virtual and real photons are indicated by, respectively, q and q'. x is the average longitudinal-momentum fraction of the struck parton, and 2ξ is the difference of longitudinal-momentum fractions between the initial and the final parton. $t = (p - p')^2$ is the squared four-momentum transfer between the initial and final nucleon.

mation. Precisely, the virtuality Q^2,

$$Q^2 = -q^2 = -(k - k')^2, \tag{1}$$

of the exchanged photon between the lepton and the nucleon must be sufficiently large for the reaction to happen at the parton level ($Q^2 \gg M^2$), and much larger than the squared four-momentum transfer to the target t,

$$t = (p - p')^2, \tag{2}$$

$(|t|/Q^2 \ll 1)$. Finally, the squared hadronic center-of-mass energy $W = (p+q)^2$ must be large, for fixed values of the Bjorken variable x_B, defined as

$$x_B = \frac{Q^2}{2M\nu}, \qquad (3)$$

where M is the proton mass and $\nu = E_e - E_{e'}$. In these conditions, the cross section of the DVCS process can be expressed as a convolution of a hard partonic subprocess, that is calculable in perturbative theory, and a soft nucleon-structure part, parametrized by the GPDs.

At leading order in α_S and at leading twist, the GPDs depend upon three variables, x, ξ, and t, where the skewness ξ is related to x_B,

$$\xi \simeq \frac{x_B}{2 - x_B}. \qquad (4)$$

Considering only quark-helicity-conserving processes, which are dominant for DVCS, at leading order and at leading twist the reaction is described by four GPDs, H^f, $\widetilde{H}^f$, E^f, $\widetilde{E}^f$ (where f stands for a light quark or for a gluon g, in which case the DVCS diagram differs from that of fig. 1), that account for the possible combinations of relative orientations of nucleon spin and parton helicity between the initial and final states. The GPDs H and E do not depend on the parton helicity and are therefore called unpolarized GPDs, while $\widetilde{H}$ and $\widetilde{E}$ depend on the parton helicity and are called polarized GPDs. The GPDs H and $\widetilde{H}$ conserve the spin of the nucleon, whereas E and $\widetilde{E}$ correspond to a nucleon-spin flip.

At $\xi = 0$, the Fourier transform of the t-dependence of a GPD provides the spatial distribution in the transverse plane for partons having a longitudinal-momentum fraction x [10].

Model-independent sum rules link the first moment in x of the GPDs to the elastic form factors (FFs) [3]:

$$\int_{-1}^{1} \mathrm{d}x\, H^q(x,\xi,t) = F_1^q(t); \quad \int_{-1}^{1} \mathrm{d}x\, E^q(x,\xi,t) = F_2^q(t);$$

$$\int_{-1}^{1} \mathrm{d}x\, \widetilde{H}^q(x,\xi,t) = G_A^q(t); \quad \int_{-1}^{1} \mathrm{d}x\, \widetilde{E}^q(x,\xi,t) = G_P^q(t), \qquad (5)$$

where $F_1^q(t)$ and $F_2^q(t)$ are the quark contributions to the Dirac and Pauli FFs, and $G_A^q(t)$ and $G_P^q(t)$ are the quark contributions to the axial and pseudoscalar FFs.

In the forward limit ($t \to 0$), the second moment in x of the sum of the GPDs H and E is linked to the total angular momentum carried by the quarks, J_q, via Ji's sum rule [3]:

$$\sum_q \int_{-1}^{+1} \mathrm{d}x\, x[H^q(x,\xi,t=0) + E^q(x,\xi,t=0)] = 2J_q. \qquad (6)$$

The DVCS final state is indistinguishable from that of the well-known Bethe-Heitler (BH) process in which the final-state photon is radiated by the incoming or scattered lepton and not by the nucleon itself. The two processes interfere, and the cross section of the hard exclusive leptoproduction of a real photon is proportional to the squared photon-production amplitude

$$|T|^2 = |T_{\mathrm{DVCS}}|^2 + |T_{\mathrm{BH}}|^2 + \underbrace{T_{\mathrm{DVCS}}T_{\mathrm{BH}}^* + T_{\mathrm{DVCS}}^*T_{\mathrm{BH}}}_{\mathrm{I}}, \qquad (7)$$

where I denotes the interference term. Given that the nucleon form factors are well known at small t, the BH amplitude T_{BH} is precisely calculable theoretically.

The DVCS amplitude is proportional to a linear combination of integrals over x of the form:

$$\int_{-1}^{1} \mathrm{d}x F(x,\xi,t) \left[\frac{1}{x - \xi - i\epsilon} \mp \frac{1}{x + \xi - i\epsilon} \right], \qquad (8)$$

where F represents a generic nucleon GPD and the top and bottom signs apply, respectively, to the unpolarized GPDs (H, E) and to the polarized GPDs $(\widetilde{H}, \widetilde{E})$. Each of these 4 integrals, which are called Compton Form Factors (CFFs), can be decomposed into its real and imaginary parts, as

$$\Re\mathrm{e}\mathcal{F} = \sum_q e_q^2 \mathcal{P} \int_{-1}^{1} \mathrm{d}x \left[\frac{1}{x - \xi} \mp \frac{1}{x + \xi} \right] F^q(x,\xi,t), \qquad (9)$$

$$\Im\mathrm{m}\mathcal{F}(\xi,t) = -\pi \sum_q e_q^2 [F^q(\xi,\xi,t) \mp F^q(-\xi,\xi,t)], \qquad (10)$$

where $\mathcal{P}$ is Cauchy's principal value integral. Therefore, at leading order and at leading twist the maximum information that can be extracted from the experimental data at a given (ξ,t) point is either $F(\pm\xi,\xi,t)$, if one measures an observable sensitive to the imaginary part of the DVCS amplitude, or $\int_{-1}^{+1} \frac{\mathrm{d}x F(\mp x,\xi,t)}{x \pm \xi}$, if one measures an observable sensitive to the real part of the DVCS amplitude.

In summary, at leading order and leading twist, in the quark sector eight GPD-related quantities can be extracted from DVCS: the real and imaginary parts of the four CFFs, defined in eqs. (9) and (10). The CFFs depending only on ξ and t, a model input is necessary to deconvolute the x-dependence of the GPDs.

In the next sections, the sensitivity to the various CFFs of the DVCS observables presented in this paper will be outlined, following the notation of ref. [18].

2 Observables for exclusive photon leptoproduction

The total cross section for exclusive photon leptoproduction, for all possible combinations of beam and target polarizations, is given by

$$\begin{aligned}
\mathrm{d}\sigma \sim\; & \mathrm{d}\sigma_{UU}^{\mathrm{BH}} + e_\ell \mathrm{d}\sigma_{UU}^{\mathrm{I}} + \mathrm{d}\sigma_{UU}^{\mathrm{DVCS}} \\
& + e_\ell P_\ell \mathrm{d}\sigma_{LU}^{\mathrm{I}} + P_\ell \mathrm{d}\sigma_{LU}^{\mathrm{DVCS}} \\
& + e_\ell S_L \mathrm{d}\sigma_{UL}^{\mathrm{I}} + S_L \mathrm{d}\sigma_{UL}^{\mathrm{DVCS}} \\
& + e_\ell S_\perp \mathrm{d}\sigma_{UT}^{\mathrm{I}} + S_\perp \mathrm{d}\sigma_{UT}^{\mathrm{DVCS}} \\
& + P_\ell S_L \mathrm{d}\sigma_{LL}^{\mathrm{BH}} + e_\ell P_\ell S_L \mathrm{d}\sigma_{LL}^{\mathrm{I}} + P_\ell S_L \mathrm{d}\sigma_{LL}^{\mathrm{DVCS}} \\
& + P_\ell S_\perp \mathrm{d}\sigma_{LT}^{\mathrm{BH}} + e_\ell P_\ell S_\perp \mathrm{d}\sigma_{LT}^{\mathrm{I}} + P_\ell S_\perp \mathrm{d}\sigma_{LT}^{\mathrm{DVCS}}. \qquad (11)
\end{aligned}$$
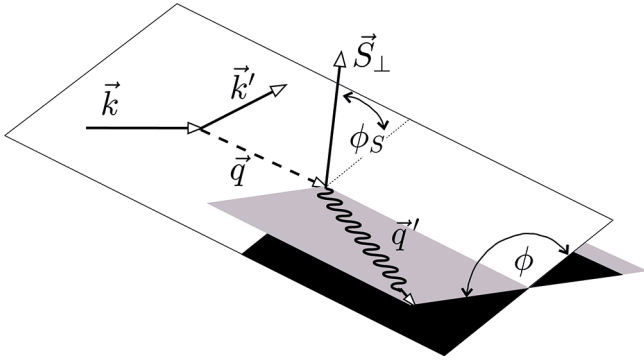
Fig. 2. Scheme illustrating the definition of the angles ϕ, formed by the leptonic and hadronic planes, and ϕ_S formed by the lepton scattering plane and $\vec{S}_\perp$, the component of the target polarization vector that is orthogonal to $\vec{q}$.

This equation follows [19] from eq. (64) of ref. [20], and also from the explicit formulae in [13,21–23].

Note that for simplicity $d\sigma$ is used instead of fourfold differential $d^4\sigma(lN \to lN\gamma)/dx_B\, dQ^2\, d|t|\, d\phi$ or, in case of transversely polarized target, instead of fivefold differential $d^5\sigma(lN \to lN\gamma)/dx_B\, dQ^2\, d|t|\, d\phi\, d\phi_S$. Here, ϕ is the angle between the lepton scattering plane and the photon production plane spanned by the virtual and real photons, as shown in fig. 2, while ϕ_S is the angle between the lepton scattering plane and $\vec{S}_\perp$, the component of the target polarization vector that is orthogonal to $\vec{q}$. These definitions are consistent with the Trento conventions [24] and differ from those used in refs. [13,21–23]: $\phi = \pi - \phi_{[13]}$ and $\phi - \phi_S = \pi + \varphi_{[13]}$.

The first subscript of the cross section σ_{XY} refers to the beam polarization state while the second refers to the target polarization state. U stands for unpolarized, L for longitudinal and T for transverse polarizations. P_ℓ and e_ℓ are the helicity and the charge of the lepton beam, respectively, and S_L is the component of the target polarization vector that is parallel to $\vec{q}$. Equation (11) consists of three parts, representing the contributions of BH (first column), the DVCS process (third column), and their interference (I, the second column). The first row of eq. (11) represents the spin-independent cross sections, rows 2–4 the single-spin–dependent cross sections, and rows 5-6 the double-spin–dependent cross sections.

All terms contributing to the exclusive photon lepto-production cross section have been expanded by Belitsky, Mueller, and Kirchner [13,21–23] up to twist-3 in Fourier series in ϕ. In the case of a transversely polarized target the expansion is done also as a function of $\phi - \phi_S$. The Fourier expansions of the individual terms in eq. (11) are given below:

$$d\sigma_{UU}^{\mathrm{BH}} = \frac{K_{\mathrm{BH}}}{\mathcal{P}_1(\phi)\,\mathcal{P}_2(\phi)} \sum_{n=0}^{2} c_{n,\mathrm{unp}}^{\mathrm{BH}} \cos(n\phi), \tag{12}$$

$$d\sigma_{UU}^{\mathrm{I}} = \frac{-K_{\mathrm{I}}}{\mathcal{P}_1(\phi)\,\mathcal{P}_2(\phi)} \sum_{n=0}^{3} c_{n,\mathrm{unp}}^{\mathrm{I}} \cos(n\phi), \tag{13}$$

$$d\sigma_{UU}^{\mathrm{DVCS}} = \frac{1}{Q^2} \sum_{n=0}^{2} c_{n,\mathrm{unp}}^{\mathrm{DVCS}} \cos(n\phi), \tag{14}$$

$$d\sigma_{LU}^{\mathrm{I}} = \frac{-K_{\mathrm{I}}}{\mathcal{P}_1(\phi)\,\mathcal{P}_2(\phi)} \sum_{n=1}^{2} s_{n,\mathrm{unp}}^{\mathrm{I}} \sin(n\phi), \tag{15}$$

$$d\sigma_{LU}^{\mathrm{DVCS}} = \frac{1}{Q^2} s_{1,\mathrm{unp}}^{\mathrm{DVCS}} \sin\phi, \tag{16}$$

$$d\sigma_{UL}^{\mathrm{I}} = \frac{-K_{\mathrm{I}}}{\mathcal{P}_1(\phi)\,\mathcal{P}_2(\phi)} \sum_{n=1}^{3} s_{n,\mathrm{LP}}^{\mathrm{I}} \sin(n\phi), \tag{17}$$

$$d\sigma_{UL}^{\mathrm{DVCS}} = \frac{1}{Q^2} \sum_{n=1}^{2} s_{n,\mathrm{LP}}^{\mathrm{DVCS}} \sin(n\phi), \tag{18}$$

$$d\sigma_{UT}^{\mathrm{I}} = \frac{-K_{\mathrm{I}}}{\mathcal{P}_1(\phi)\mathcal{P}_2(\phi)} \left\{ \sum_{n=0}^{3} c_{n,\mathrm{TP-}}^{\mathrm{I}} \sin(\phi - \phi_S) \cos(n\phi) \right. \\ \left. + \sum_{n=1}^{3} s_{n,\mathrm{TP+}}^{\mathrm{I}} \cos(\phi - \phi_S) \sin(n\phi) \right\}, \tag{19}$$

$$d\sigma_{UT}^{\mathrm{DVCS}} = \frac{1}{Q^2} \left\{ \sum_{n=0}^{2} c_{n,\mathrm{TP-}}^{\mathrm{DVCS}} \sin(\phi - \phi_S) \cos(n\phi) \right. \\ \left. + \sum_{n=1}^{2} s_{n,\mathrm{TP+}}^{\mathrm{DVCS}} \cos(\phi - \phi_S) \sin(n\phi) \right\}, \tag{20}$$

$$d\sigma_{LL}^{\mathrm{BH}} = \frac{K_{\mathrm{BH}}}{\mathcal{P}_1(\phi)\,\mathcal{P}_2(\phi)} \sum_{n=0}^{1} c_{n,\mathrm{LP}}^{\mathrm{BH}} \cos(n\phi), \tag{21}$$

$$d\sigma_{LL}^{\mathrm{I}} = \frac{-K_{\mathrm{I}}}{\mathcal{P}_1(\phi)\,\mathcal{P}_2(\phi)} \sum_{n=0}^{2} c_{n,\mathrm{LP}}^{\mathrm{I}} \cos(n\phi), \tag{22}$$

$$d\sigma_{LL}^{\mathrm{DVCS}} = \frac{1}{Q^2} \sum_{n=0}^{1} c_{n,\mathrm{LP}}^{\mathrm{DVCS}} \cos(n\phi), \tag{23}$$

$$d\sigma_{LT}^{\mathrm{BH}} = \frac{K_{\mathrm{BH}}}{\mathcal{P}_1(\phi)\,\mathcal{P}_2(\phi)} \left\{ \sum_{n=0}^{1} c_{n,\mathrm{TP}}^{\mathrm{BH}} \cos(\phi - \phi_S) \cos(n\phi) \right. \\ \left. + s_{1,\mathrm{TP}}^{\mathrm{BH}} \sin(\phi - \phi_S) \sin\phi \right\}, \tag{24}$$

$$d\sigma_{LT}^{\mathrm{I}} = \frac{-K_{\mathrm{I}}}{\mathcal{P}_1(\phi)\mathcal{P}_2(\phi)} \left\{ \sum_{n=0}^{2} c_{n,\mathrm{TP+}}^{\mathrm{I}} \cos(\phi - \phi_S) \cos(n\phi) \right. \\ \left. + \sum_{n=1}^{2} s_{n,\mathrm{TP-}}^{\mathrm{I}} \sin(\phi - \phi_S) \sin(n\phi) \right\}, \tag{25}$$

$$d\sigma_{LT}^{\mathrm{DVCS}} = \frac{1}{Q^2} \left\{ \sum_{n=0}^{1} c_{n,\mathrm{TP+}}^{\mathrm{DVCS}} \cos(\phi - \phi_S) \cos(n\phi) \right. \\ \left. + s_{1,\mathrm{TP-}}^{\mathrm{DVCS}} \sin(\phi - \phi_S) \sin\phi \right\}. \tag{26}$$

The terms K_{BH} and K_{I} are kinematic factors: $K_{\mathrm{BH}} = 1/(x_B^2 \, t \, (1 + \epsilon^2)^2)$ and $K_{\mathrm{I}} = 1/(x_B \, y \, t)$, where y is the fraction of the beam energy carried by the virtual photon in the target rest frame and $\epsilon \equiv 2 x_B M_N / Q$, with M_N the nucleon mass. The subscript "unp" stands for unpolarized, "LP" for longitudinally and "TP" for transversely polarized targets. An additional subscript $\pm$ is used for DVCS and interference terms, TP+ (TP−), containing $\cos(\phi - \phi_S)$ ($\sin(\phi - \phi_S)$).

The Fourier coefficients $c_{n,\mathrm{unp}}^{\mathrm{BH}}$ and the lepton propagators $\mathcal{P}_1(\phi), \mathcal{P}_2(\phi)$ of the BH term can be calculated within the framework of QED from the kinematic variables and the Dirac and Pauli form factors, F_1 and F_2.

The single-spin–dependent coefficients of the interference term are proportional to the imaginary parts of the CFFs, while the unpolarized and double-spin–dependent coefficients are connected to the real parts of the CFFs.

The Fourier coefficients of the interference term are of great interest since they depend on a linear combination of CFFs, while the coefficients of the squared DVCS term are bilinear in the CFFs. The quantitative access to the Fourier coefficients of the interference term is complicated by the presence of DVCS terms, the Fourier coefficients of which have the same azimuthal dependences as the ones of the interference term. This entanglement can be resolved by taking into account the explicit dependence of the interference terms on the lepton beam charge e_ℓ (see eq. (11)).

2.1 Unpolarized and helicity-dependent cross sections with polarized lepton beams

Using lepton beams of a given charge e_ℓ but with opposite polarizations, the sum and the difference of the cross sections are built as:

$$\frac{1}{2}(\mathrm{d}\sigma^{\rightarrow} + \mathrm{d}\sigma^{\leftarrow}) = \mathrm{d}\sigma_{UU}^{\mathrm{BH}} + \mathrm{d}\sigma_{UU}^{\mathrm{DVCS}} + e_\ell \mathrm{d}\sigma_{UU}^{\mathrm{I}}, \quad (27)$$

$$\frac{1}{2}(\mathrm{d}\sigma^{\rightarrow} - \mathrm{d}\sigma^{\leftarrow}) = \mathrm{d}\sigma_{LU}^{\mathrm{DVCS}} + e_\ell \mathrm{d}\sigma_{LU}^{\mathrm{I}}. \quad (28)$$

Here, $\sigma^{\rightarrow}$ ($\sigma^{\leftarrow}$) denotes the cross section for a beam with positive (negative) helicity. The Fourier expansion of the cross sections is given in eqs. (12)–(16). Contributing at higher twist, the DVCS terms $\mathrm{d}\sigma_{UU}^{\mathrm{DVCS}}$ and $\mathrm{d}\sigma_{LU}^{\mathrm{DVCS}}$ are suppressed compared to the interference terms $\mathrm{d}\sigma_{UU}^{\mathrm{I}}$ and $\mathrm{d}\sigma_{LU}^{\mathrm{I}}$, respectively. Among all harmonic coefficients, the ones which at leading twist and at leading order are expected to be dominant in the sum (eq. (27)) and difference (eq. (28)) of cross sections are, respectively:

$$c_{1,\mathrm{unp}}^{\mathrm{I}}, \qquad s_{1,\mathrm{unp}}^{\mathrm{I}}.$$

The dominant part of the coefficient $c_{1,\mathrm{unp}}^{\mathrm{I}}$ is proportional to a linear combination of the real parts of CFFs containing quark-helicity-conserving twist-2 GPDs,

$$c_{1,\mathrm{unp}}^{\mathrm{I}} \propto \Re\mathrm{e}\left[F_1 \mathcal{H} + \xi(F_1 + F_2)\widetilde{\mathcal{H}} - \frac{t}{4M^2}F_2 \mathcal{E}\right], \quad (29)$$

while the dominant part of the coefficient $s_{1,\mathrm{unp}}^{\mathrm{I}}$ is proportional to an analogous linear combination of the imaginary parts of the same CFFs:

$$s_{1,\mathrm{unp}}^{\mathrm{I}} \propto \Im\mathrm{m}\left[F_1 \mathcal{H} + \xi(F_1 + F_2)\widetilde{\mathcal{H}} - \frac{t}{4M^2}F_2 \mathcal{E}\right]. \quad (30)$$

The kinematic factors ξ and t being small, the measurements of unpolarized cross section and helicity-dependent cross section difference on a proton target will be mainly sensitive to, respectively, $\Re\mathrm{e}\mathcal{H}$ and $\Im\mathrm{m}\mathcal{H}$, since $F_1 > F_2$. The measurements on a neutron target will provide, instead, sensitivity to $\Re\mathrm{e}\mathcal{E}$ and $\Im\mathrm{m}\mathcal{E}$, as F_1 is negligible compared to F_2 in this case.

The kinematically suppressed coefficient $c_{0,\mathrm{unp}}^{\mathrm{I}}$ is directly proportional to $c_{1,\mathrm{unp}}^{\mathrm{I}}$ via a kinematic factor originating from the BH propagators:

$$c_{0,\mathrm{unp}}^{\mathrm{I}} \propto -\frac{\sqrt{-t}}{Q} c_{1,\mathrm{unp}}^{\mathrm{I}}. \quad (31)$$

At kinematics where BH becomes negligible with respect to DVCS, the coefficient $c_{0,\mathrm{unp}}^{\mathrm{DVCS}}$ also comes into play. It is related to a bilinear combination of the 4 CFFs, among which $(\mathcal{H}\mathcal{H}^* + \widetilde{\mathcal{H}}\widetilde{\mathcal{H}}^*)$ is the dominant one [13, 21–23].

The other coefficients in eqs. (12)–(16) are related to combinations of CFFs of either higher-twist or helicity-flip GPDs. Details are given in refs. [13, 21–23]. In the following subsections only the dominant harmonic coefficients sensitive to quark-helicity-conserving twist-2 GPDs will be discussed.

2.2 Charge difference and charge-averaged cross sections with polarized lepton beams

Using positive (+) and negative (−) lepton beams with opposite polarizations, the sum of the cross sections,

$$\frac{1}{2}\left(\mathrm{d}\sigma^{\overset{+}{\rightarrow}} + \mathrm{d}\sigma^{\overset{-}{\leftarrow}}\right) = \mathrm{d}\sigma_{UU}^{\mathrm{BH}} + \mathrm{d}\sigma_{UU}^{\mathrm{DVCS}} + \mathrm{d}\sigma_{LU}^{\mathrm{I}}, \quad (32)$$

or their difference,

$$\frac{1}{2}\left(\mathrm{d}\sigma^{\overset{+}{\rightarrow}} - \mathrm{d}\sigma^{\overset{-}{\leftarrow}}\right) = \mathrm{d}\sigma_{LU}^{\mathrm{DVCS}} + \mathrm{d}\sigma_{UU}^{\mathrm{I}}, \quad (33)$$

allow the separation between the squared-DVCS and interference terms, as they have different azimuthal modulations, containing either $\cos n\phi$ or $\sin n\phi$.

These observables select the 3 harmonic coefficients,

$$c_{0,\mathrm{unp}}^{\mathrm{I}}, \qquad c_{1,\mathrm{unp}}^{\mathrm{I}}, \qquad s_{1,\mathrm{unp}}^{\mathrm{I}},$$

discussed in the previous section.

2.3 Beam-charge asymmetry

The measurement of the cross section asymmetry with respect to the beam charge, not taking into account the beam polarization,

$$A_C(\phi) \equiv \frac{d\sigma^+ - d\sigma^-}{d\sigma^+ + d\sigma^-} = \frac{d\sigma_{UU}^I}{d\sigma_{UU}^{BH} + d\sigma_{UU}^{DVCS}}, \qquad (34)$$

is a way to single out the interference term in the numerator. The Fourier expansion of $d\sigma_{UU}^I$ is given in eq. (13). The $d\sigma_{UU}^{DVCS}$ term in the denominator has a $1/Q^2$ kinematic suppression (see eq. (14)). The dominant coefficient of BH term $d\sigma_{UU}^{BH}$ is $c_{0,unp}^{BH}$. However, the coefficient of the $\cos\phi$ term is also, often, not small.

The dominant coefficients, at leading twist, are $c_{1,unp}^I$ and $c_{0,unp}^I$ (see eqs. (29) and (31)) discussed in sect. 2.1.

2.4 Beam-spin asymmetries

Measurements with a longitudinally polarized lepton beam of a certain charge on an unpolarized target provide access, at leading twist, to $s_{1,unp}^I$ via the single-charge beam-helicity asymmetry, also called beam-spin asymmetry (BSA):

$$A_{LU}(\phi, e_\ell) \equiv \frac{d\sigma^\rightarrow - d\sigma^\leftarrow}{d\sigma^\rightarrow + d\sigma^\leftarrow}$$
$$= \frac{e_\ell d\sigma_{LU}^I + d\sigma_{LU}^{DVCS}}{d\sigma_{UU}^{BH} + e_\ell d\sigma_{UU}^I + d\sigma_{UU}^{DVCS}}. \qquad (35)$$

The access to $s_{1,unp}^I$ is complicated by the presence of two leading-twist Fourier coefficients, $c_{1,unp}^I$ and $c_{0,unp}^I$, in the denominator.

This entanglement can be avoided using longitudinally polarized lepton beams of both charges. Two beam-spin asymmetries can then be defined: the charge-difference beam-helicity asymmetry,

$$A_{LU}^I(\phi) \equiv \frac{(d\sigma^{+\rightarrow} - d\sigma^{+\leftarrow}) - (d\sigma^{-\rightarrow} - d\sigma^{-\leftarrow})}{(d\sigma^{+\rightarrow} + d\sigma^{+\leftarrow}) + (d\sigma^{-\rightarrow} + d\sigma^{-\leftarrow})}$$
$$= \frac{d\sigma_{LU}^I}{d\sigma_{UU}^{BH} + d\sigma_{UU}^{DVCS}}, \qquad (36)$$

and the charge-averaged beam-helicity asymmetry:

$$A_{LU}^{DVCS}(\phi) \equiv \frac{(d\sigma^{+\rightarrow} - d\sigma^{+\leftarrow}) + (d\sigma^{-\rightarrow} - d\sigma^{-\leftarrow})}{(d\sigma^{+\rightarrow} + d\sigma^{+\leftarrow}) + (d\sigma^{-\rightarrow} + d\sigma^{-\leftarrow})}$$
$$= \frac{d\sigma_{LU}^{DVCS}}{d\sigma_{UU}^{BH} + d\sigma_{UU}^{DVCS}}. \qquad (37)$$

The beam spin asymmetry A_{LU}^I is directly sensitive to the coefficient $s_{1,unp}^I$ (see eq. (15)) giving access to the imaginary part of the CFFs in eq. (30). There is no leading-twist contribution to the charge-averaged asym-

metry A_{LU}^{DVCS} (see eq. (16)).

The relation between the asymmetries discussed above (eq. (35) on one hand and eqs. (34), (36), (37) on the other) is

$$A_{LU}(\phi, e_\ell) = \frac{e_\ell A_{LU}^I(\phi) + A_{LU}^{DVCS}(\phi)}{1 + e_\ell A_C(\phi)}. \qquad (38)$$

2.5 Longitudinal target-spin asymmetries

Up to this point, only unpolarized targets were considered. It is essential to extract as many observables as possible to be able to disentangle the four GPDs. The use of polarized targets (together with polarized beams) gives a possibility to measure a large variety of additional observables.

Measuring DVCS off a longitudinally polarized target and with an unpolarized lepton beam allows the extraction of the target-spin asymmetry A_{UL} (here also referred to as TSA):

$$A_{UL}(\phi, e_\ell) \equiv \frac{d\sigma^\Rightarrow - d\sigma^\Leftarrow}{d\sigma^\Rightarrow + d\sigma^\Leftarrow}$$
$$\equiv \frac{[d\sigma^{\leftarrow\Rightarrow} + d\sigma^{\rightarrow\Rightarrow}] - [d\sigma^{\leftarrow\Leftarrow} + d\sigma^{\rightarrow\Leftarrow}]}{[d\sigma^{\leftarrow\Rightarrow} + d\sigma^{\rightarrow\Rightarrow}] + [d\sigma^{\leftarrow\Leftarrow} + d\sigma^{\rightarrow\Leftarrow}]}$$
$$= \frac{e_\ell d\sigma_{UL}^I + d\sigma_{UL}^{DVCS}}{d\sigma_{UU}^{BH} + e_\ell d\sigma_{UU}^I + d\sigma_{UU}^{DVCS}}. \qquad (39)$$

Here, $\Rightarrow$ ($\Leftarrow$) represents the target polarization state parallel (antiparallel) to the beam momentum. The Fourier expansion of the terms in the numerator is given in eqs. (17) and (18). The Fourier coefficient of interest in this case is

$$s_{1,LP}^I \propto \Im m\left[F_1\widetilde{\mathcal{H}} + \xi(F_1 + F_2)\left(\mathcal{H} + \frac{x_B}{2}\mathcal{E}\right)\right.$$
$$\left. - \xi\left(\frac{x_B}{2}F_1 + \frac{t}{4M^2}F_2\right)\widetilde{\mathcal{E}}\right]. \qquad (40)$$

In the case of a proton target, the dominant contribution to A_{UL} comes from $\Im m\widetilde{\mathcal{H}}_p$ and, in a minor way, from $\Im m\mathcal{H}_p$, that is from the GPDs $\widetilde{H}_p$ and H_p along the lines $x = \pm\xi$ [13, 21–23]. A measurement of both the TSA and BSA is needed to truly distinguish between the two GPDs. In the neutron case, for which $F_2 \gg F_1$, this observable is mostly sensitive to $\Im m\mathcal{H}_n$.

2.6 Transverse target-spin asymmetries

Experimental observables that provide sensitivity to the coefficients appearing in eqs. (19) and (20) are the single-spin asymmetries in the cross section for scattering of

a lepton beam off a transversely polarized target:

$$A_{UT}^{\mathrm{DVCS}}(\phi, \phi_S) \equiv \frac{1}{S_\perp}$$

$$\times \frac{\mathrm{d}\sigma^+(\phi,\phi_S)-\mathrm{d}\sigma^+(\phi,\phi_S+\pi)+\mathrm{d}\sigma^-(\phi,\phi_S)-\mathrm{d}\sigma^-(\phi,\phi_S+\pi)}{\mathrm{d}\sigma^+(\phi,\phi_S)+\mathrm{d}\sigma^+(\phi,\phi_S+\pi)+\mathrm{d}\sigma^-(\phi,\phi_S)+\mathrm{d}\sigma^-(\phi,\phi_S+\pi)}$$

$$= \frac{\mathrm{d}\sigma_{UT}^{\mathrm{DVCS}}}{\mathrm{d}\sigma_{UU}^{\mathrm{BH}} + \mathrm{d}\sigma_{UU}^{\mathrm{DVCS}}}, \tag{41}$$

$$A_{UT}^{\mathrm{I}}(\phi, \phi_S) \equiv \frac{1}{S_\perp}$$

$$\times \frac{\mathrm{d}\sigma^+(\phi,\phi_S)-\mathrm{d}\sigma^+(\phi,\phi_S+\pi)-\mathrm{d}\sigma^-(\phi,\phi_S)+\mathrm{d}\sigma^-(\phi,\phi_S+\pi)}{\mathrm{d}\sigma^+(\phi,\phi_S)+\mathrm{d}\sigma^+(\phi,\phi_S+\pi)+\mathrm{d}\sigma^-(\phi,\phi_S)+\mathrm{d}\sigma^-(\phi,\phi_S+\pi)}$$

$$= \frac{\mathrm{d}\sigma_{UT}^{\mathrm{I}}}{\mathrm{d}\sigma_{UU}^{\mathrm{BH}} + \mathrm{d}\sigma_{UU}^{\mathrm{DVCS}}}. \tag{42}$$

The extraction of A_{UT}^{I} gives an access to the Fourier coefficient

$$c_{1,\mathrm{TP-}}^{\mathrm{I}} \propto -\frac{M}{Q} \Im m \left\{ \frac{t}{4M^2} \left[(2 - x_B) F_1 \mathcal{E} - 4\frac{1-x_B}{2-x_B} F_2 \mathcal{H} \right] \right.$$

$$\left. + 1 x_B \xi \left[F_1 (\mathcal{H} + \mathcal{E}) - (F_1 + F_2)\left(\widetilde{\mathcal{H}} + \frac{t}{4M^2}\widetilde{\mathcal{E}} \right) \right] \right\}, \tag{43}$$

which, on a proton target, provides a rare access to the CFF $\Im m \mathcal{E}$ with no kinematic suppression of its contribution relative to those of the other CFFs.

The other coefficients of interest are

$$c_{0,\mathrm{TP-}}^{\mathrm{I}} \propto -\frac{\sqrt{-t}}{Q} c_{1,\mathrm{TP-}}^{\mathrm{I}}, \tag{44}$$

with approximately the same dependence on the CFFs as $c_{1,\mathrm{TP-}}^{\mathrm{I}}$, and

$$c_{0,\mathrm{TP-}}^{\mathrm{DVCS}} \propto -\frac{\sqrt{-t}}{M} \Im m \left\{ \mathcal{H}\mathcal{E}^* - \mathcal{E}\mathcal{H}^* + \xi \widetilde{\mathcal{E}}\,\widetilde{\mathcal{H}}^* - \xi \widetilde{\mathcal{H}}\,\widetilde{\mathcal{E}}^* \right\}, \tag{45}$$

also providing an access to the CFF $\Im m \mathcal{E}$ (due to additional kinematic prefactors which partially compensate the strong kinematic suppression of the squared-DVCS amplitude relative to the interference term).

2.7 Double-spin asymmetries

The use of a polarized lepton beam along with either a longitudinally or a transversely polarized target allows also the determination of the double-spin asymmetries (also referred to as DSA in the following) A_{LL} or A_{LT}. Unlike in the case of the single-spin asymmetries A_{UL}, A_{LU} and A_{UT}, the BH process alone can generate a double-spin asymmetry (see eq. (11)). All the three contributions, BH, DVCS, and their interference, have the same azimuthal harmonics (see eqs. (21)–(23) and eqs. (24)–(26)). The contribution of the interference terms can be separated from those of pure DVCS and BH in measurements using both beam charges. As for the DVCS term, its Fourier

coefficients are indistinguishable from those of BH. Nevertheless, the BH coefficients can be calculated from the measured elastic form factors.

In case of longitudinally polarized target, the asymmetry A_{LL} is given as

$$A_{LL}(\phi, e_\ell) \equiv \frac{[\mathrm{d}\sigma^{\rightarrow\Rightarrow} + \mathrm{d}\sigma^{\leftarrow\Leftarrow}] - [\mathrm{d}\sigma^{\leftarrow\Rightarrow} + \mathrm{d}\sigma^{\rightarrow\Leftarrow}]}{[\mathrm{d}\sigma^{\rightarrow\Rightarrow} + \mathrm{d}\sigma^{\leftarrow\Leftarrow}] + [\mathrm{d}\sigma^{\leftarrow\Rightarrow} + \mathrm{d}\sigma^{\rightarrow\Leftarrow}]}$$

$$= \frac{\mathrm{d}\sigma_{LL}^{\mathrm{BH}} + e_\ell \mathrm{d}\sigma_{LL}^{\mathrm{I}} + \mathrm{d}\sigma_{LL}^{\mathrm{DVCS}}}{\mathrm{d}\sigma_{UU}^{\mathrm{BH}} + e_\ell \mathrm{d}\sigma_{UU}^{\mathrm{I}} + \mathrm{d}\sigma_{UU}^{\mathrm{DVCS}}}. \tag{46}$$

The constant and the $\cos\phi$-dependent terms contain mixed contributions from BH, DVCS and their interference. Nonetheless, it is expected that in some parts of the phase space A_{LL} has a measurable sensitivity to $\Re e \widetilde{\mathcal{H}}_p$ and, in a lesser way, $\Re e \mathcal{H}_p$, for the proton-target case, and to $\Re e \mathcal{H}_n$ for the neutron, since

$$c_{0,\mathrm{LP}}^{\mathrm{I}}, c_{1,\mathrm{LP}}^{\mathrm{I}} \propto \Re e \left[F_1 \widetilde{\mathcal{H}} + \xi(F_1 + F_2)\left(\mathcal{H} + \frac{x_B}{2}\mathcal{E} \right) \right.$$

$$\left. -\xi\left(\frac{x_B}{2}F_1 + \frac{t}{4M^2}F_2 \right)\widetilde{\mathcal{E}} \right]. \tag{47}$$

For brevity, the experimental definitions of the beam-charge-difference and charge-averaged double-spin asymmetries, A_{LT}^{I} and $A_{LT}^{\mathrm{BH+DVCS}}$, on a transversely polarized target are not shown here. They can be found in [25]. They give access to the coefficients in eqs. (24)–(26). Among them the dominant ones contributing to the beam-charge-difference asymmetry

$$A_{LT}^{\mathrm{I}}(\phi, \phi_S) = \frac{\mathrm{d}\sigma_{LT}^{\mathrm{I}}}{\mathrm{d}\sigma_{UU}^{\mathrm{BH}} + \mathrm{d}\sigma_{UU}^{\mathrm{DVCS}}} \tag{48}$$

are

$$c_{0,\mathrm{TP+}}^{\mathrm{I}}, c_{1,\mathrm{TP+}}^{\mathrm{I}}, s_{1,\mathrm{TP-}}^{\mathrm{I}},$$

providing information on the real parts of linear combinations of four CFFs ($\mathcal{H}$, $\mathcal{E}$, $\widetilde{\mathcal{H}}$ and $\widetilde{\mathcal{E}}$):

$$c_{1,TP+}^{I} \propto -\frac{M}{Q}$$

$$\times \Re e \left\{ \frac{t}{4M^2} \left[4\frac{1-x_B}{2-x_B} F_2 \widetilde{\mathcal{H}} - (F_1 + \xi F_2)x_B \widetilde{\mathcal{E}} \right] \right.$$

$$\left. + x_B \left[(F_1 + F_2)\left(\xi\mathcal{H} + \frac{t}{4M^2}\mathcal{E} - \xi F_1\left(\widetilde{\mathcal{H}} + \frac{x_B}{2}\widetilde{\mathcal{E}} \right) \right) \right] \right\}, \tag{49}$$

$$s_{1,TP-}^{I} \propto -\frac{M}{Q} \Re e \left\{ \frac{t}{4M^2} \left[(2-x_B)F_1 \mathcal{E} - 4\frac{1-x_B}{2-x_B} F_2 \mathcal{H} \right] \right.$$

$$\left. + x_B \xi \left[F_1(\mathcal{H} + \mathcal{E}) - (F_1 + F_2)\left(\widetilde{\mathcal{H}} + \frac{t}{4M^2}\widetilde{\mathcal{E}} \right) \right] \right\}, \tag{50}$$

$$c_{0,TP+}^{I} \propto -\frac{t}{\sqrt{Q}} c_{1,TP+}^{I}. \tag{51}$$
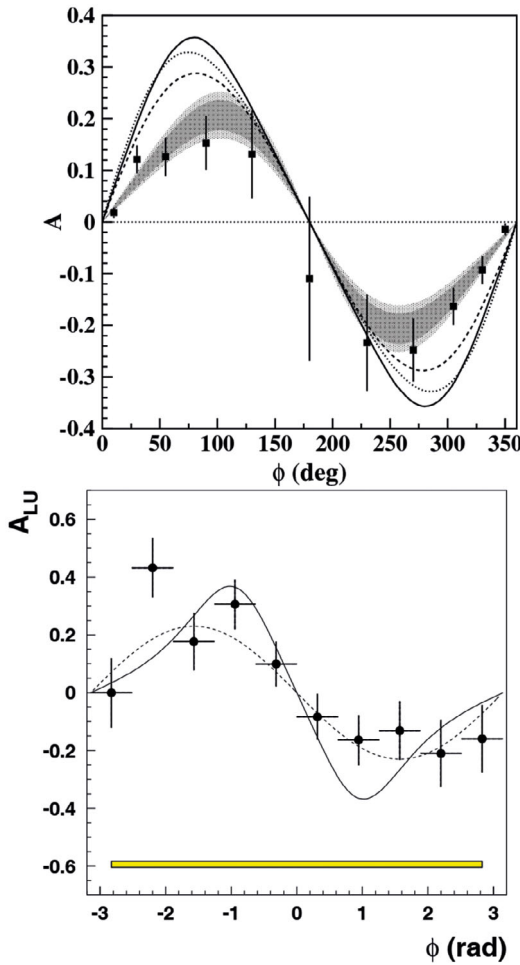
Fig. 3. First measurement of the ϕ-dependence of the DVCS beam-spin asymmetry from CLAS [26] with an electron beam (top), at $\langle Q^2 \rangle = 1.25\,\mathrm{GeV}^2$, $\langle x_B \rangle = 0.19$, and $\langle -t \rangle = 0.19\,\mathrm{GeV}^2$, and from HERMES [27] with a positron beam (bottom), at $\langle Q^2 \rangle = 2.6\,\mathrm{GeV}^2$, $\langle x_B \rangle = 0.11$, and $\langle -t \rangle = 0.27\,\mathrm{GeV}^2$. Top: the dark shaded region is the range of the fitted function $A(\phi) = \alpha \sin \phi + \beta \sin 2\phi$ defined by the statistical errors of the α and β parameters, the light shaded region includes systematic uncertainties added linearly to the statistical uncertainties. The curves are model calculations from [28] and [11]. Bottom: The dashed curve represents a $\sin \phi$-dependence with an amplitude of 0.23, while the solid curve represents the result of a model calculation taken from ref. [29]. The horizontal error bars represent the bin width, and the error band below represents the systematic uncertainty.

3 DVCS experiments in the world

Among all exclusive processes, DVCS has the cleanest theoretical interpretation in terms of GPDs. However, experimental measurements of DVCS are quite challenging, as they require:

- high enough luminosities to measure small cross sections;
- polarized lepton beams of both charges, and/or polarized targets to measure observables having sensitivity to different combinations of CFFs;

- detectors capable to ensure the exclusivity of the final state.

It is clearly a highly non-trivial task to actually measure the GPDs. It calls for a long-term experimental program comprising the measurements of different DVCS observables on proton and on neutron targets, as well as using different lepton beam energies, and performing experiments on different kinematic coverages.

Such a dedicated experimental program has advanced worldwide in these past few years, mostly on proton targets. After the first observations of the $\sin \phi$-dependence for $ep \to e'p'\gamma$ events —a signature expected from the interference of the DVCS and BH processes— in low-statistics beam-spin asymmetry measurements [26,27] (see fig. 3), various DVCS measurements, also with high statistics, have been performed.

As of today, the HERMES experiment provided the most complete set of DVCS observables due to its flexibility with regard to

- beam charges (e^+ and e^-);
- beam helicities (both longitudinal polarizations);
- target-spin variations (longitudinal, transverse, unpolarized);
- recoil proton detection.

These measurements, which will be described in the following sections, are an important input for the parametrizations of GPDs and their extraction via global fits. The variety of experimental conditions made the HERMES experiment rather unique. HERMES stopped the data taking in 2007 and currently no new measurements are planned.

Thanks to the high energy available in collider mode at HERA (27 GeV electron beam against 920 proton beams) the H1 [30–33] and ZEUS [34,35] were able to measure the "pure" DVCS cross sections, without BH contribution, and were able to study accurately their evolution as a function of Q^2, W, and t, for kinematics where sea quarks and gluon exchanges dominate ($10^{-4} < x_B < 10^{-2}$). Details about these results will be provided in the following.

After the first publication by CLAS in 2001, a series of high-statistics DVCS-dedicated experiments followed at Jefferson Lab, at moderate Q^2 (1–3 GeV^2) and in a x_B range (centered around $x_B \sim 0.3$) corresponding to the valence-quarks region. As of today, the polarized and unpolarized cross sections measured at Jefferson Lab in Hall A indicate, via a Q^2-scaling test, that the factorization and the hypothesis of leading-twist dominance are valid already at relatively low Q^2 ($\sim$ 1–2 GeV^2). High-statistics and finely binned fourfold beam-spin asymmetries measured in Hall B with CLAS brought important constraints for the study of the GPD H on a wide kinematic range.

These first sets of data are being expanded and completed with the results from more recent JLab experiments and analyses for DVCS on the proton, aimed to measure accurately fully differential beam-polarized cross section differences and unpolarized cross sections, longitudinally polarized target-spin asymmetries along with double polarization observables.

An energy upgrade to 12 GeV of the CEBAF accelerator of JLab was completed in 2014, and the capabilities of the detectors in the halls A, B, and C are being enhanced to suit the new experimental program, which will have a particular focus on the study of Generalized Parton Distributions. Covering a range in x_B from 0.1 to 0.7 and in Q^2 from 1 to 10 GeV^2, the upgraded JLab will be very well matched to study GPDs in the valence regime. The first experiment of the 12 GeV era is presently running in Hall A and focuses on proton DVCS: beam-polarized and unpolarized cross sections will be measured with high precision at three electron-beam energies to increase the kinematical coverage of the previous measurements [36], perform an accurate Q^2-scaling test, and extract the squared-DVCS and the interference terms of the cross section via a Rosenbluth separation. The experimental program for the first 5 years of operation of CLAS12 (the new Hall-B detector, currently under completion) will be particularly focused on measurements of GPDs in exclusive processes. Measurements of beam-spin asymmetries, unpolarized and polarized proton-DVCS cross sections, as well as TSA and DSA with longitudinally polarized targets and single- and double-spin asymmetries on transversely polarized targets are planned. A similar experimental program is being defined for DVCS on the neutron.

A major part of the future COMPASS program [37] is dedicated to investigating the structure of the nucleon by studying GPDs through DVCS and DVMP. The availability of muon beams with high energy and opposite charge and polarization will allow to disentangle the interference terms and the squared-DVCS contributions, and to reach the real and the imaginary parts of the dominant CFF, the one of the GPD H. A measurement of the x_B-dependence of the t slope of the pure DVCS cross section will be done to study nucleon tomography. COMPASS will collect data in a kinematic domain yet unexplored ($0.005 < x_B < 0.3$), between HERMES and the JLab experiments on the one hand, and the HERA collider experiments on the other hand.

All these results and planned measurements will be discussed in detail in the following sections. For details on the GPD models that will be presented along with the data, see ref. [18] (in this Topical Issue).

4 Pure DVCS cross section on an unpolarized proton target

Experiments which run in collider mode and/or with very energetic lepton beams can achieve energies high enough that the DVCS contribution becomes dominant with respect to the contributions of BH and of the interference. Thus the study of the pure DVCS cross section is possible. This was done at H1 and ZEUS, with a 27 GeV electron beam colliding against a 920 GeV proton beam, and is underway at COMPASS using the 160 GeV muon beam of the SPS at CERN.

H1 [30–33] and ZEUS [35,38] covered a large domain of x_B ranging from 10^{-4} to 10^{-2}. At such small values of x_B, two-gluon exchange (fig. 4) plays a major role in addition to the leading-order quark-photon scattering process.
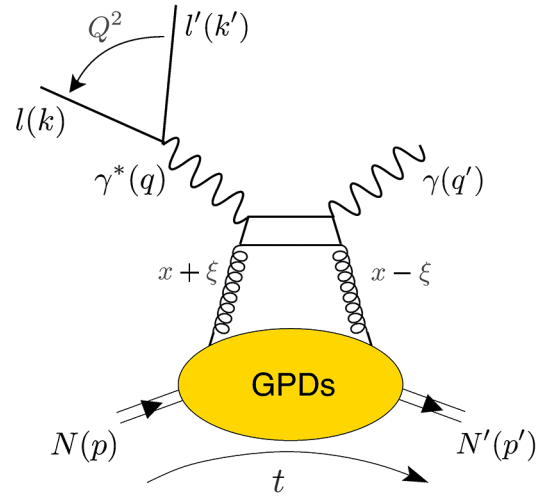

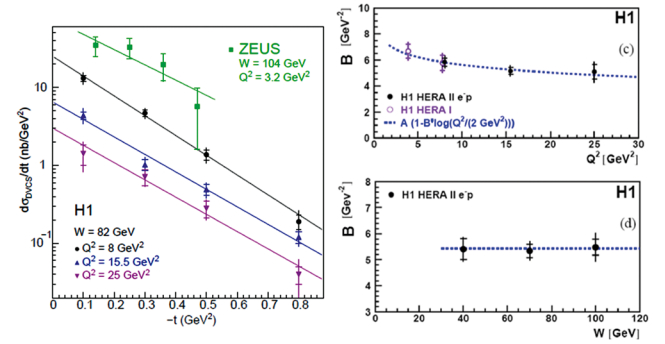**Fig. 4.** DVCS diagram for two-gluon exchange.

Fig. 5. Left: the t-dependence of the DVCS cross section for four values of Q^2, as measured by H1 and ZEUS. The curves are the results of fits of the form $e^{-B|t|}$. Right: the fitted B values as a function of Q^2 (top) and W (bottom). The curves represent the result of the fit $B(Q^2) = A(1 - B' \log(Q^2/2 \, \text{GeV}^2))$ (top) and the average value $B = 5.45 \, \text{GeV}^{-2}$ (bottom). Figure from ref. [32].

The behavior of the differential cross section as a function of W and t follows the Regge formalism and can be parametrized as:

$$\mathrm{d}\sigma/\mathrm{d}t \propto e^{-B(W)|t|} \tag{52}$$

with

$$B(W) = B_0 + 4\alpha' \ln(W/W_0), \tag{53}$$

where B_0 and W_0 are constants. The value of α' has been found to be rather small for DVCS. This is in constrast with a non-zero value of α' observed in exclusive meson production [39,40], which has provided an interplay between the t and W dependencies of the differential cross section. When the value of W increases, B increases as well, which means that the scattering object gets bigger: this phenomenon, called "shrinkage", is not observed for the DVCS cross section at HERA kinematics.

Figure 5 (left panel) shows the differential cross section $\mathrm{d}\sigma/\mathrm{d}t$, for different Q^2 ranges, measured at H1 [32] and ZEUS [38], integrated over W. The behavior of the data is
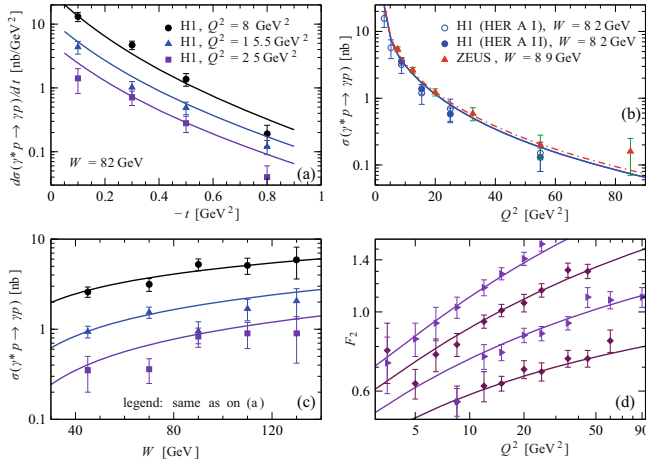
Fig. 6. Simultaneous fit to the DVCS and DIS data in the $\overline{\text{CS}}$ scheme at NNLO. First three panels: DVCS cross section measured at H1 [31,32] and ZEUS [35] as a function of t, Q^2 and W. Last panel: $F_2(x_B, Q^2)$ *versus* Q^2 for $x_B = 8.0 \; 10^{-3}$, $3.2 \; 10^{-3}$, $1.3 \; 10^{-3}$, $5.0 \; 10^{-4}$, going from the upper curve to the lower one [43]. Figure from ref. [42].

well described by the exponential (eq. (52)), and the parameter B of the t-slope is presented on the right panel. There is no significant dependence on W for B (right bottom panel). The Q^2-dependence (right top panel) can be parametrized as $B(Q^2) = A(1 - B' \log(Q^2/2 \, \text{GeV}^2))$ with $A = 6.98 \pm 0.54 \, \text{GeV}^2$ and $B' = 0.12 \pm 0.03 \, \text{GeV}^2$. The average slope is $B = 5.45 \pm 0.19_{stat} \pm 0.34_{syst} \, \text{GeV}^{-2}$ at $\langle Q^2 \rangle = 8 \, \text{GeV}^2$. This can be translated into the transverse extension of the parton distributions in the proton using the relation

$$\langle r_\perp^2(x_B) \rangle \approx 2 \cdot B(x_B), \tag{54}$$

which is valid at small x_B. Thus, a transverse extension of sea quarks and gluons in the proton [32] of $\sqrt{\langle r_T^2 \rangle} = 0.65 \pm 0.02 \, \text{fm}$ has been measured at an average value of $x_B = 1.2 \; 10^{-3}$. This can be compared to the transverse charge radius of the proton $\sqrt{\langle r_T^2 \rangle}_{ch}$ given by $\sqrt{4 \frac{\mathrm{d}}{\mathrm{d}t} F_1^p|_{t=0}} = 0.67 \pm 0.01 \, \text{fm}$ [41].

The HERA data from both H1 and ZEUS are well reproduced by the GPD model developed by Kumericki and Mueller [42]. They proposed a flexible parametrization of the GPDs (noted KM09). It is based on both a Mellin-Barnes integral and dispersion integral representation with weakly entangled skewness and t-dependences. Figure 6 presents the rather good quality of a simultaneous fit to the DVCS cross sections as a function of Q^2, W and t measured at HERA [31,32,35], and DIS data [43]. The fit is performed in the special conformal scheme ($\overline{\text{CS}}$) to NNLO accuracy [42].

Thanks to the high energy of the muon beam available at COMPASS [37], the DVCS cross section can also be extracted, after BH subtraction and integration of the remaining azimuthal dependence (see eqs. (32) and (33)). Figure 7 (on top) shows the projected statistical accuracy for a measurement of the x_B-dependence of the t-slope parameter $B(x_B)$ of the DVCS cross section, in 40
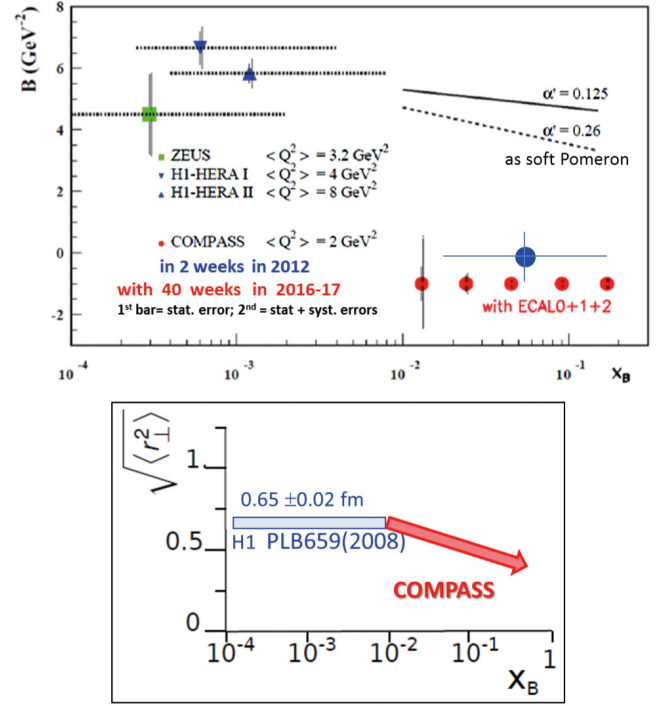

Fig. 7. Top: projections, for 40 weeks of running time in 2016-2017, for the x_B-dependence of the t-slope parameter $B(x_B)$ of the DVCS cross section, calculated for $1 < Q^2 < 8 \, \text{GeV}^2$. A comparison to results from HERA with similar $\langle Q^2 \rangle$ is shown. The left vertical bar on each data point indicates the statistical error only while the right one includes also the systematic uncertainty. The blue point indicates the statistical error which can be reached using the pilot run done in 2012. Two different parameterizations are shown, using $\alpha' = 0.125 \, \text{GeV}^{-2}$ and $0.26 \, \text{GeV}^{-2}$. Bottom: transverse proton radius as a function of x_B from HERA and COMPASS.

weeks of running time in 2016 and 2017 at COMPASS. At small x_B, no evolution with x_B was observed at HERA (fig. 5, right panel). In the valence region, where no experimental determinations of B exist, some information comes from fits adjusted to form factor data which give $\alpha' \simeq 1 \, \text{GeV}^2$ [44,45]. The COMPASS predictions were made using the HEPGen Monte Carlo generator for exclusive events. The model relies on a non-factorizable (Reggeized) t-dependence for the DVCS amplitude. For the simulation, two values $\alpha' = 0.125$ and $\alpha' = 0.26$ are shown, which correspond to the half and the total of the value for Pomeron exchange in soft scattering processes [40]. These values can be determined at COMPASS with an accuracy better than 2.5σ. This will provide information on the evolution of the transverse size of the nucleon (eq. (54)) over the uncharted x_B-range from 0.01 to 0.1 (see fig. 7, bottom) an important issue to advance in the "tomography" of the nucleon.

5 Unpolarized, helicity-dependent, and helicity-and-charge–dependent cross sections

As explained in sect. 2, DVCS observables can be expressed as linear and bilinear combinations of CFFs, elec-
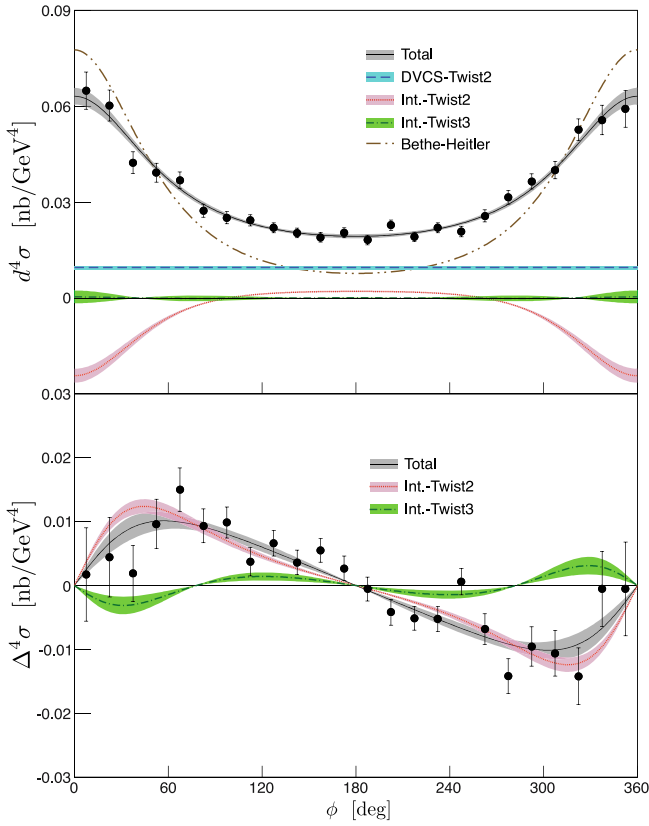
Fig. 8. Hall A results, for Kin3, $t = 0.32\,\text{GeV}^2$: unpolarized (top) and helicity-dependent (bottom) cross section as a functions of ϕ. The error bars on the data points are statistical only. The shaded areas represent the statistical uncertainty for each contribution. This figure is from ref. [46].

tromagnetic form factors, and terms depending on the kinematics. The study, at fixed Q^2, x_B, $-t$, of the ϕ-dependence of DVCS cross sections, cross section differences, and asymmetries can help single out the contributions from the various CFFs. Fourfold $(Q^2, x_B, -t, \phi)$ differential cross sections, unpolarized and beam-polarized, for the exclusive electroproduction of photons were recently measured at Jefferson Lab, by the Hall A and the CLAS Collaborations. The imminent experiments at COMPASS will aim to extract the real part of $\mathcal{H}$ by measuring helicity-and-charge–dependent cross sections differences.

5.1 Hall A results

E00-110, the first experiment specifically dedicated to DVCS, ran in Hall A at Jefferson Lab during the year 2004, with the primary goal of performing a Q^2-scaling test of the DVCS cross section. Polarized electrons, accelerated to 5.7572 GeV by the CEBAF accelerator, impinged on a 15 cm long liquid-hydrogen target. The data, first published in 2006 [36], were recently reanalyzed [46], and the new results now supersede the old ones. The exclusivity of the $e p \gamma$ final state was ensured by detecting the scattered electrons in the High Resolution Spectrometer, the
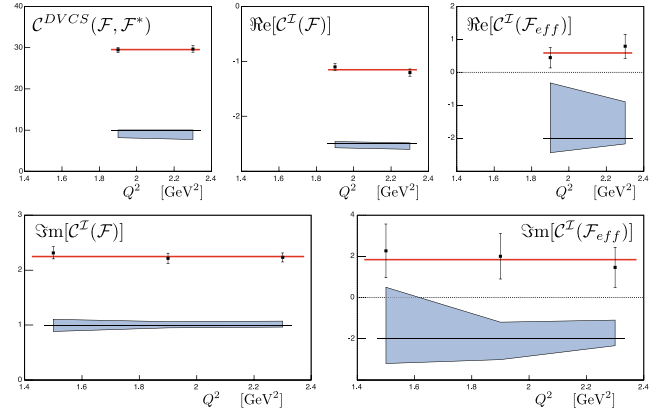
Fig. 9. Combinations of effective CFFs extracted from the Hall-A data using the formalism developed in [22], integrated over t and plotted as a function of Q^2. The top three plots show the effective CFFs resulting from the unpolarized cross section fit (Kin2 and Kin3), whereas the bottom plots show the effective CFFs resulting from the helicity-dependent cross section fit (Kin1–3). The shaded areas represent systematic errors. Figure taken from ref. [46].

DVCS/BH photons in a custom-built PbF_2 electromagnetic calorimeter, and reconstructing the recoil protons via the $ep \to e\gamma X$ missing mass. $ep\gamma$ events were collected for five different (Q^2, x_B) kinematics: Kin1 ($Q^2 = 1.5\,\text{GeV}^2$, $x_B = 0.36$), Kin2 ($Q^2 = 1.9\,\text{GeV}^2$, $x_B = 0.36$), and Kin3 ($Q^2 = 2.3\,\text{GeV}^2$, $x_B = 0.36$), with constant x_B and varying Q^2; KinX2 ($Q^2 = 2.06\,\text{GeV}^2$, $x_B = 0.39$) and KinX3 ($Q^2 = 2.17\,\text{GeV}^2$, $x_B = 0.34$), with fixed Q^2 but varying x_B. Each of these five (Q^2, x_B) kinematics was further differentiated in 5 $-t$ bins and 24 ϕ bins, and fourfold unpolarized and beam-polarized cross sections were extracted. Figure 8 shows the obtained results for the $-t = 0.32\,\text{GeV}^2$ bin of Kin3. The unpolarized cross sections peak towards $\phi = 0°$ due to the BH process (dot-dashed gray curves). The different contributions to the cross section (DVCS, Bethe-Heitler, Interference), shown in color, were separated, up to twist three for the interference term, using the BMK formalism [22]. This method also allowed the extraction of five observables linked to combinations of real and imaginary parts of CFFs: $\mathcal{C}^{\text{DVCS}}(\mathcal{F}, \mathcal{F}^*)$ (bilinear in the CFFs, obtained from the $c_{0,\text{unp}}^{\text{DVCS}}$ harmonic), $\Re e[\mathcal{C}^I(\mathcal{F})]$ (linear in the CFFs, obtained from $c_{1,\text{unp}}^I$, eq. (29)), and $\Re e[\mathcal{C}^I(\mathcal{F}_{eff})]$ (twist-three term, from $c_{2,\text{unp}}^I$ [22]) are extracted from the unpolarized cross section, while the helicity-dependent cross section is fitted using the $\Im m[\mathcal{C}^I(\mathcal{F})]$ (linear in the CFFs, obtained from $s_{1,\text{unp}}^I$, eq. (30)) and $\Im m[\mathcal{C}^I(\mathcal{F}_{eff})]$ (twist-three term, from $s_{2,\text{unp}}^I$ [22]).

The constant Q^2-dependence of the five observables (fig. 9) confirms that the factorization and leading-twist approximations for DVCS are valid already at these relatively low Q^2 (~ 1–$2\,\text{GeV}^2$), as first observed in the previous analysis of these same data [36].
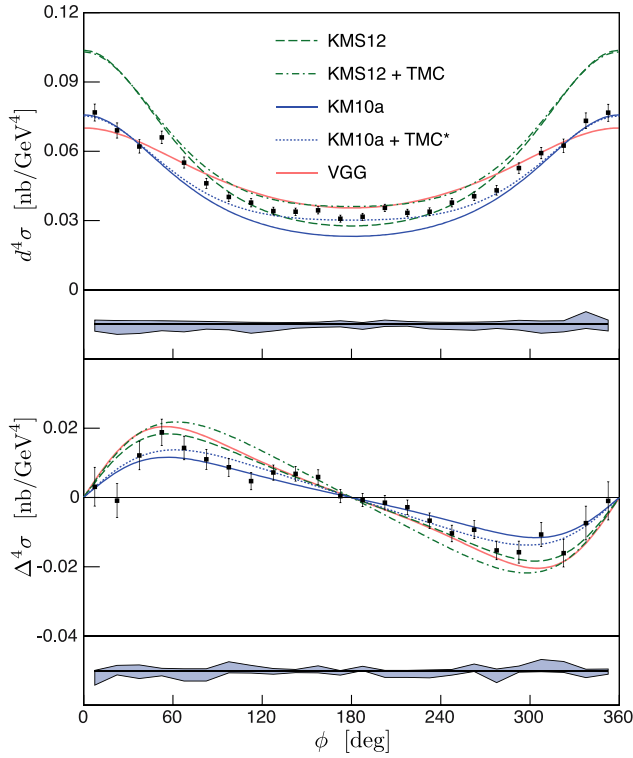
Fig. 10. Unpolarized (top) and helicity-dependent (bottom) cross sections for the Hall-A Kin2 bin, $t = 0.23\,\mathrm{GeV}^2$. The light blue area represents the point-to-point systematic uncertainties added linearly to the normalization error. The predictions from the KMS12 and VGG models are shown as the dashed green and solid red curves, respectively. The KM10a fit is represented as the solid blue line. Target-mass and finite-t corrections are included in the KMS12 model and shown as the dotted-dash curve. The correction is then applied to the KM10a model shown as the dotted blue line. Figure from ref. [46].

In fig. 10, the results are compared to double-distribution GPD models (VGG [11,28,45,47] and KMS12 [48]) and fits to previous data. Unlike VGG, the KMS12 model was tuned using vector meson data at low to very-low x_B, and may be not optimal for the valence-quark region. Both models tend to overestimate the helicity-dependent cross sections in this kinematics, while VGG reproduces better the unpolarized data. The data are also compared to the KM10a model [42], which reproduces very well the helicity-dependent data but underestimates significantly the DVCS unpolarized cross section around $\phi = 180°$. Adding an empirical estimate of the target-mass and finite-t corrections to the KM10a model improves the agreement with the data significantly, while it seems to worsen it for the KMS12 model. Such effects are not fully understood at this stage, and they may be clarified with the analysis of the new data coming from JLab experiments at 12 GeV, such as the one described in the next section.

5.2 Hall A experiment at 11 GeV

A new DVCS experiment, with similar setup of E00-110 but using the upgraded CEBAF accelerator, has recently
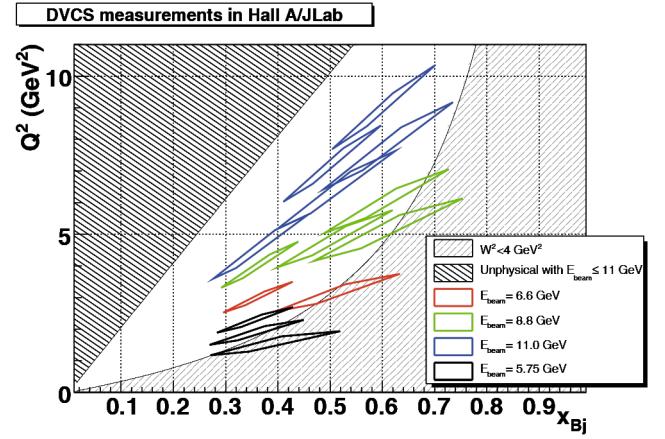

Fig. 11. DVCS kinematics for $\mathrm{H}(e, e'\gamma)p$ measurements in Hall A with 3, 4, and 5 pass beams of CEBAF at 12 GeV. The diamond shapes trace the approximate acceptance of the HRS in each setting. The boundary of the unphysical region corresponds to the maximum possible Q^2 at a given x_B for 11 GeV. This corresponds to 180° electron scattering, equivalent to $\theta_q = 0°$. The points at $E_{\mathrm{Beam}} = 5.75\,\mathrm{GeV}$ were obtained in E00-110. Figure taken from ref. [49].
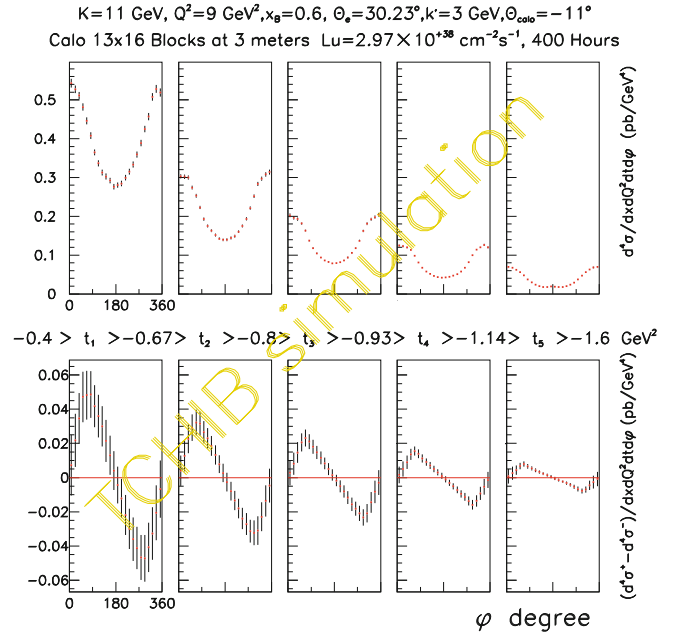
Fig. 12. Projected DVCS cross sections (top) and beam-helicity differences for the ongoing Hall-A experiment, for the setting with $k = 11\,\mathrm{GeV}$ (where k here indicates the beam energy), $Q^2 = 9\,\mathrm{GeV}^2$, $x_B = 0.6$, as a function of ϕ for 5 bins in $-t$. Figure from ref. [49].

started running in Hall A at Jefferson Lab [49]. It will measure the $\vec{e}p \to ep\gamma$ cross sections at fixed x_B over as wide a range in Q^2 as possible for beam energies $E_e \le 11\,\mathrm{GeV}$ (fig. 11), by using three different electron-energy settings. The study of the Q^2-dependence of the DVCS cross sections will determine at what level the "handbag" amplitude dominates, or not, over the higher-twist amplitudes.
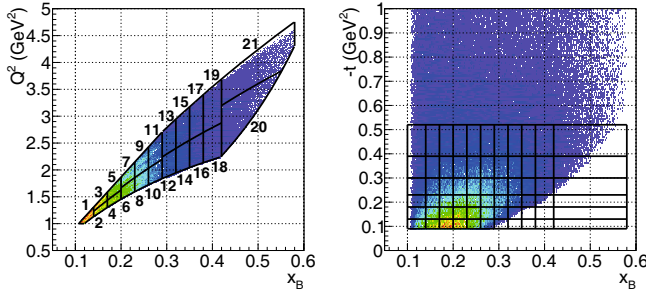
Fig. 13. The (Q^2, x_B) and $(-t, x_B)$ kinematic coverages of the CLAS E01-113 experiment, with the corresponding binning. Figure from ref. [53].

The expected accuracy for the absolute cross sections and beam-helicity cross section differences, for the 11 GeV beam-energy setting as an example, is shown in fig. 12. The obtained results will allow to extract five kinematically independent CFF-related quantities, for each Q^2, x_B, t point, which are angular harmonic superpositions of Compton Form Factors as functions of ϕ, similarly to what was done for E00-110 (see fig. 9). Each of these five quantities isolates the real or the imaginary part of a distinct combination of linear $(BH \cdot DVCS^\dagger)$ and bilinear $(DVCS \cdot DVCS^\dagger)$ terms.

The t-dependence of each angular harmonic term will also be measured. Changes in the t-dependence of the extracted observables as a function of x_B are expected. In particular, the $r.m.s.$ impact parameter of a quark of momentum fraction x must diminish as a power of $(1-x)$ as $x \to 1$. This is expected to be a sizeable effect: between $x = 0.36$ and $x = 0.6$ it leads to a change in t slope of a factor of two for the individual GPDs. The precision and coverage of the data currently being taken in Hall A will allow to study such effects. A similar experiment, which will complement the kinematic coverage of the Hall A, is also planned in Hall C at Jefferson Lab [50].

5.3 CLAS results

The E01-113 experiment took place at JLab during three months in 2005, using the CEBAF 5.75 GeV polarized electron beam (79.4% polarization), a 2.5 cm long liquid hydrogen target, and the Hall B large-acceptance CLAS spectrometer [51], operating at a luminosity of $2 \cdot 10^{34}$ cm^2 s^{-1}. The polar-angle acceptance of CLAS for photons (15–45°) was extended down to 5° with the addition of a specially designed electromagnetic calorimeter ("inner calorimeter", IC [52]), with full azimuthal coverage. $ep\gamma$ events were detected in CLAS and in the IC, and tight cuts on missing masses and angles ensured the exclusivity of the final state. Figure 13 [53] shows the resulting (Q^2, x_B) (left) and $(-t, x_B)$ (right) kinematic coverages of the data and the adopted binning (21 (Q^2, x_B) bins and 6 $-t$ bins). The events in each $(Q^2, x_B, -t)$ bin were further divided into 24 bins in ϕ. Figure 14 shows, for two selected (Q^2, x_B) bins in different parts of the phase space, the ϕ-dependence of the $ep \to e'p'\gamma$ unpolarized
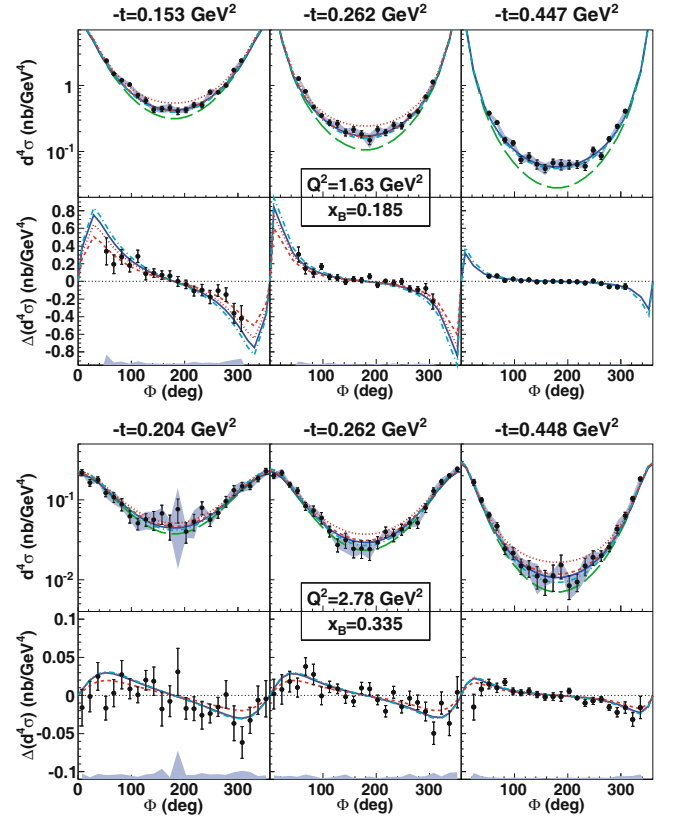

Fig. 14. Top six plots: unpolarized cross section (top row) and beam-polarized cross section difference for the $ep \to e'p'\gamma$ reaction, as a function of ϕ, for $(Q^2, x_B) = (1.63 \text{ GeV}^2, 0.185)$ and for 3 values of $-t$: 0.153, 0.262 and 0.447 GeV^2. Bottom six plots: same observables for $(Q^2, x_B) = (2.78 \text{ GeV}^2, 0.335)$ and $-t = 0.204$, 0.262 and 0.448 GeV^2. The green long-dashed curves show the BH contribution only. The other curves correspond to the predictions of four GPD models: VGG [11,28,45,47] (blue solid curves), KMS12 [48] (cyan dash-dotted curves), and two versions of the KM model [42,54], KM10 (red dotted curves) and KM10a (red short-dashed curves). The blue bands show the systematic uncertainties. Figure taken from ref. [53].

cross section (top) and beam-polarized cross section difference (bottom). For each of these (Q^2, x_B) bins, three selected $-t$ bins are shown.

As was observed in the Hall-A results (fig. 8), the BH process (green long-dashed curves in fig. 14) causes the unpolarized cross sections to peak towards $\phi = 0°$. The difference between the BH curves and the data can thus be attributed to the DVCS process. Figure 14 shows the calculations of four GPD models, described in the caption. Three of these models, VGG, KMS12, and the KM10a version of the KM model, describe the data well without additional inputs, while the KM10 model fails to reproduce the data near $\phi = 180°$. The model interpretation of the E01-113 results favors a smaller deviation from the pure BH process around $\phi = 180°$ than suggested by the Hall A data [36], that only the KM10 model manages to fit, thanks to the inclusion of a sizeable contribution of the
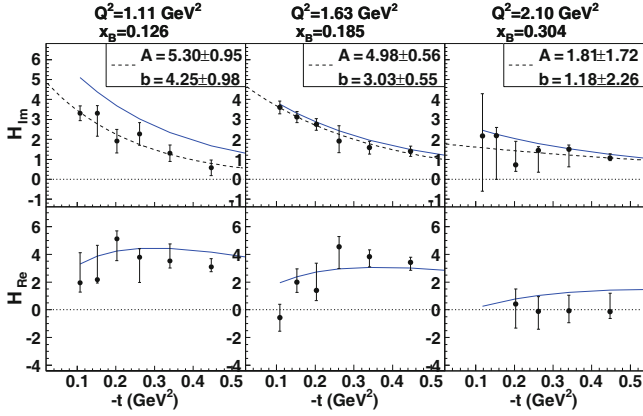
Fig. 15. Results of the CFF fit of the CLAS unpolarized and beam-polarized cross sections for H_{Im} (upper panel) and H_{Re} (lower panel), for three (Q^2, x_B) bins, as a function of t. The blue solid curves are the predictions of the VGG model. The black dashed curves show the fit of the results by the function Ae^{bt}. Figure taken from ref. [53].

GPD $\widetilde{H}$. Therefore, the CLAS results reinforce the expectation of the H-dominance in the unpolarized $ep\gamma$ cross section.

These data were also used to extract the CFFs, using the procedure described in [15,55], based on a local-fitting method at each given experimental $(Q^2, x_B, -t)$ kinematic point. In this framework, instead of the four complex CFFs defined as in eqs. (9) and (10), there are eight real CFFs defined as

$$F_{Re}(\xi, t) = \Re e \mathcal{F}(\xi, t), \qquad (55)$$

$$F_{Im}(\xi, t) = -\frac{1}{\pi} \Im m \mathcal{F}(\xi, t) = [F(\xi, \xi, t) \mp F(-\xi, \xi, t)], \qquad (56)$$

where the sign convention is the same as for eq. (8). These CFFs are the parameters that are extracted from DVCS observables using the well-established DVCS+BH theoretical amplitude. For the fit to the CLAS cross sections, this CFF-extraction procedure was applied leaving only 4 CFFs as free parameters [53].

Figure 15 shows, for a selection of three out of the 21 (Q^2, x_B) bins, the t distribution of the fitted H_{Im} and H_{Re}. Figure 15 also shows the predictions of the VGG model, which overestimates the fitted H_{Im} at the smallest values of x_B.

The t-dependence of H_{Im} was fitted with the function Ae^{bt}, with A and b left as free parameters. Reminding that b is related to the transverse size of the nucleon, the fact that b increases with decreasing x_B suggests that the nucleon size increases at lower parton-momentum values, thus revealing from experiment a first tomographic image of the nucleon. The increase of A, instead, reflect an increase with x_B in the density of partons in the proton.

5.4 Planned cross section measurements at COMPASS

In the beam charge-and-spin difference of the cross section for unpolarized proton target, that will be measured at
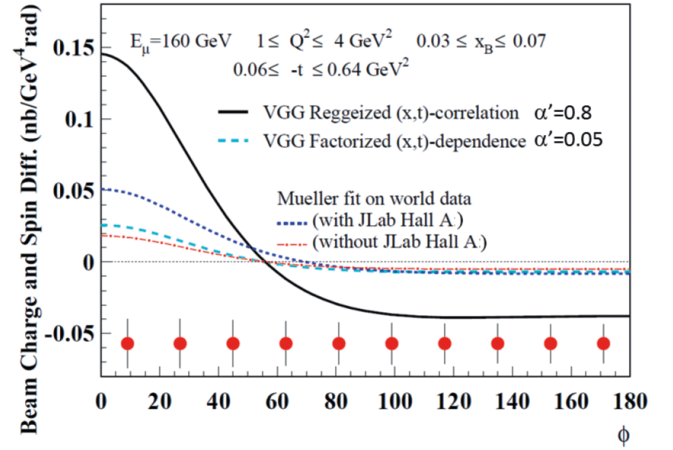
Fig. 16. Projected statistical accuracy (error bars) for a measurement of the ϕ-dependence of $d\sigma^{\overleftarrow{+}} - d\sigma^{\overrightarrow{-}}$ for $0.03 \leq x \leq 0.07$ and $1 \leq Q^2 \leq 4\,\mathrm{GeV}^2$. This corresponds to 40 weeks of running time in 2016-17 with a $2.5\,\mathrm{m}$ long LH_2 target, an intensity of $4.6 \times 10^8\,\mu$ in a $48\,\mathrm{s}$ SPS spill period and an overall global efficiency of 10%. Two model predictions are shown: VGG [11,28,45,47] (black and cyan curves on left) and a calculation from a global fit to world data [42] with (blue curve) and without (red curve) including JLab Hall A data [36]. Note that the JLab Hall A results have been superseded by the results produced by the new analysis described in sect. 5.1. Figure from ref. [37].

COMPASS [37], the contribution from BH cancels out, as was shown in eq. (33), and

$$d\sigma^{\overrightarrow{+}} - d\sigma^{\overleftarrow{-}} \propto c_{0,\mathrm{unp}}^{\mathrm{I}} + c_{1,\mathrm{unp}}^{\mathrm{I}} \cos\phi. \qquad (57)$$

In eq. (57) the DVCS amplitude is expanded in $1/Q$ keeping only leading-twist terms [13, 21–23]. The coefficients $c_{0,\mathrm{unp}}^{\mathrm{I}}$ and $c_{1,\mathrm{unp}}^{\mathrm{I}}$ are, for COMPASS kinematics, dominated by the real part of $\mathcal{H}$.

Figure 16 shows the projected statistical accuracy in one bin for 40 weeks of running time planned for 2016 and 2017. The bin corresponds to the kinematics $x_B \sim 0.05$, $Q^2 \sim 2\,\mathrm{GeV}^2$, for the complete range in $-t$ ($0.06 < -t < 0.64\,\mathrm{GeV}^2$).

The black and cyan curves are predictions using the VGG model [11, 28, 45, 47] and 2 shrinkage parameters α' of 0.8 or 0.05 where the large value is well adapted for the valence region. The red and blue curves are calculations from a global fit to world data done by Kumericki and Mueller [42] with (blue) and without (red) including JLab Hall A 2006 results [36]. Note that the JLab Hall A results have now been superseded by new results described in sect. 5.1.

Figure 17 presents the $\cos\phi$ modulation of the asymmetry, integrated over Q^2 as a function of t in 6 domains in x_B. This modulation is related to the real part of the CFF $\mathcal{H}$ which was found positive at HERA [34] close to zero at CLAS [53], and negative at HERMES [56]. The kinematic domain of COMPASS, in particular the region $0.005 < x_B < 0.03$ (see the 3 top panels of fig. 17) is ex-
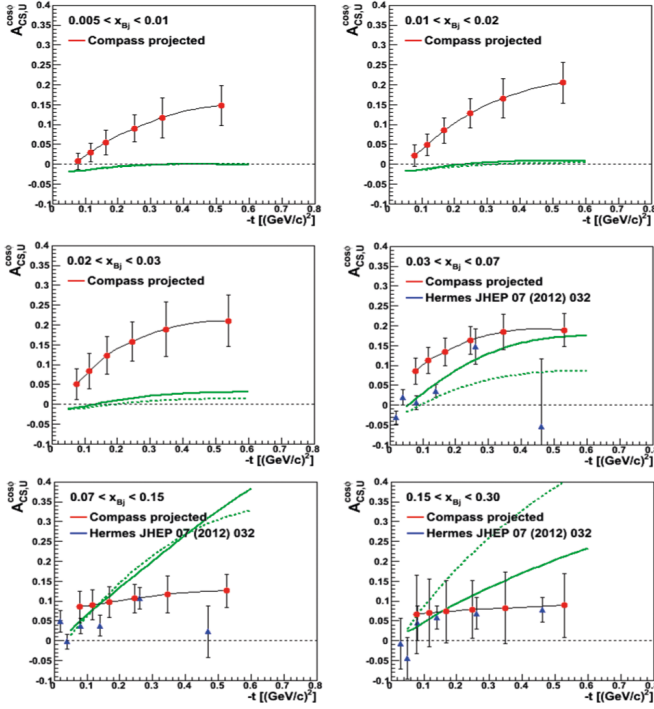
Fig. 17. Projected statistical accuracy for the amplitude of the $\cos\phi$ modulation of the beam charge-and-spin asymmetry which will be measured at COMPASS [37] in 40 weeks of running time in 2016-17. The projections (red points) are calculated using the VGG model [11,28,45,47]. The green curves show recent calculations [42] based on a global fit of world data including JLab Hall A (solid line) or not (dotted line). The blue triangles at large x_B show results from HERMES [56].

pected to allow the determination of the x_B position of the node of this function, which is an essential input for any global fitting procedure of GPDs.

6 DVCS asymmetries for unpolarized proton target

At HERMES kinematics the DVCS process makes only a small contribution to the photon production cross section compared to the BH contribution. Thus the basic concept at HERMES is to measure the interference term and get an access to the DVCS amplitudes through measurements of asymmetries with respect to the charge and helicity of the incident lepton and/or the polarization of the target.

The main features of the DVCS experiments carried out at CLAS, instead, are, on the one hand, the reconstruction of the $ep\gamma$ final state via the detection of all three particles, which minimizes systematic uncertainties due to the presence of backgrounds, and, on the other hand, the extraction of four-dimensional asymmetries with good accuracy and on a vast kinematical coverage. This provides stringent constraints for GPD models and fit-based CFF extraction methods.

6.1 Separation of contributions from DVCS and its interference with the BH process at HERMES

In the case of an unpolarized target and a longitudinally polarized beam, the experimental observables that provide sensitivity to the coefficients of eqs. (13), (15), and (16) are the two sets of asymmetries, the beam-helicity asymmetries (A_{LU}^{I} and A_{LU}^{DVCS}) and beam-charge asymmetries (A_C), appearing in the distribution of the real photons in the azimuthal angle ϕ:

$$\sigma(\phi, P_\ell, e_\ell) = \sigma_{UU}(\phi)$$
$$\times \left[1 + P_\ell A_{LU}^{\mathrm{DVCS}}(\phi) + e_\ell P_\ell A_{LU}^{\mathrm{I}}(\phi) + e_\ell A_C)(\phi)\right]. \quad (58)$$

The charge-dependent terms correspond to interference terms, while the charge-independent terms correspond to squared-DVCS term. The data collected by HERMES with both beam charges and helicities, allows the separation of the individual terms in eq. (58). The expansions in ϕ of the asymmetries are given [57] by

$$A_{LU}^{\mathrm{I}}(\phi) \simeq \sum_{n=1}^{2} A_{LU,\mathrm{I}}^{\sin(n\phi)} \sin(n\phi), \quad (59)$$

$$A_{LU}^{\mathrm{DVCS}}(\phi) \simeq A_{LU,\mathrm{DVCS}}^{\sin(\phi)} \sin(\phi), \quad (60)$$

$$A_C(\phi) \simeq \sum_{n=0}^{3} A_C^{\cos(n\phi)} \cos(n\phi). \quad (61)$$

These asymmetries relate to the Fourier coefficients according to eqs. (34), (36) and (37). At HERMES kinematics, the dominant contribution to the BH term in the denominator is the constant term, to the degree that one can neglect the effects of the coefficients $c_{1,\mathrm{unp}}^{\mathrm{BH}}$ and $c_{2,\mathrm{unp}}^{\mathrm{BH}}$ and the squared unpolarized DVCS amplitude and the effect of the ϕ-dependence of the BH propagators. In any case, the extracted asymmetry amplitudes are well defined and can be computed in various GPD models for direct comparison with the data. The asymmetry amplitudes $A_{LU,\mathrm{I}}^{\sin\phi}$, $A_C^{\cos\phi}$ and $A_C^{\cos(0\phi)}$ are the ones related to twist-2 GPDs via the Fourier coefficients $c_{0,\mathrm{unp}}^{\mathrm{I}}$, $c_{1,\mathrm{unp}}^{\mathrm{I}}$, and $s_{1,\mathrm{unp}}^{\mathrm{I}}$ given in eqs. (29), (30), and (31). The asymmetry amplitudes $A_{LU,\mathrm{DVCS}}^{\sin\phi}$, $A_{LU,\mathrm{I}}^{\sin(2\phi)}$, $A_C^{\cos(2\phi)}$ and $A_C^{\cos(3\phi)}$ are related to other Fourier coefficients in eqs. (13), (15) and (16).

The simultaneous extraction of all the azimuthal amplitudes of the DVCS asymmetries at HERMES is based on a maximum-likelihood technique [58] with a bin-free fit in the azimuthal angle ϕ.

The resulting $\cos(n\phi)$ amplitudes of the beam-charge asymmetry A_C are shown on fig. 18, integrated over all kinematic variables ("Overall": $\langle -t \rangle = 0.12\,\mathrm{GeV}^2$, $x_B = 0.10$, $\langle Q^2 \rangle = 2.46\,\mathrm{GeV}^2$) and also projected against $-t$, x_B and Q^2. The overall values of the $\cos(0\phi)$ and $\cos\phi$ amplitudes are both non-zero. These amplitudes are zero at small values of $-t$ and become non-zero with increasing values of $-t$. The two amplitudes have opposite sign and $\cos(0\phi)$ has a smaller magnitude. This is the reflection of the relation between the two underlying coefficients $c_{0,\mathrm{unp}}^{\mathrm{I}}$ and $c_{1,\mathrm{unp}}^{\mathrm{I}}$ (see eq. (31)). Both amplitudes
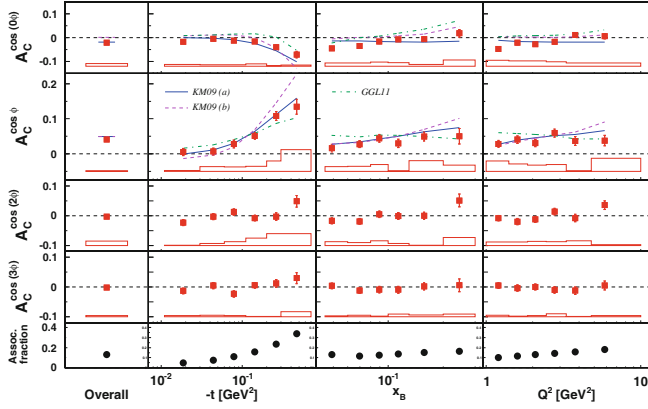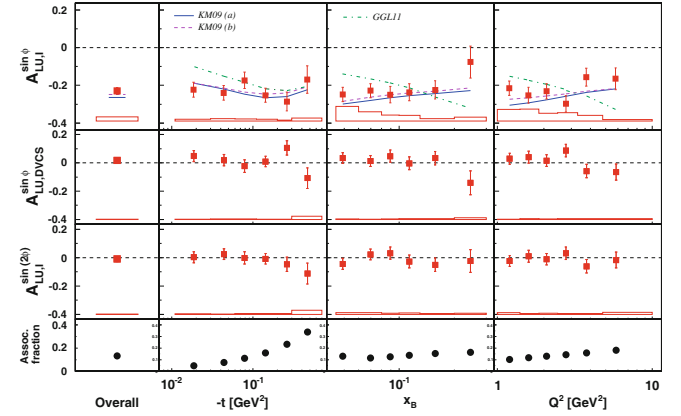
Fig. 18. The $\cos(n\phi)$ amplitudes ($n = 0$–3) of the beam-charge asymmetry A_C extracted from all the unpolarized hydrogen data recorded at HERMES from 1996 until 2007 in the entire experimental acceptance (left column), as well as a function of $-t$, x_B, and Q^2. The error bars (bands) represent the statistical (systematic) uncertainties. Solid and dashed lines (KM09) show model calculations from ref. [42]; calculations from ref. [59] are shown as dashed-dotted lines (GGL11). The simulated fractional contribution from associated production to the yield in each kinematic bin is shown in the bottom row. The figure is from ref. [60].

Fig. 19. The $A_{LU,\mathrm{I}}^{\sin\phi}$, $A_{LU,\mathrm{DVCS}}^{\sin\phi}$ and $A_{LU,\mathrm{I}}^{\sin(2\phi)}$ beam-helicity asymmetry amplitudes extracted from all the unpolarized hydrogen data recorded at HERMES from 1996 until 2007 in the entire experimental acceptance, as well as a function of $-t$, x_B, and Q^2. The error bars (bands) represent the statistical (systematic) uncertainties. An additional 3.2% scale uncertainty is present in the amplitudes due to the uncertainty of the beam polarization measurement. Solid and dashed lines (KM09) show model calculations from ref. [42]; calculations from ref. [59] are shown as dashed-dotted lines (GGL11). The simulated fractional contribution from associated production to the yield in each kinematic bin is shown in the bottom row. The figure is from ref. [60].

indicate a weak increase with x_B or Q^2. The $\cos(2\phi)$ and $\cos(3\phi)$ amplitudes, which are related to twist-3 GPDs and gluon helicity-flip GPDs, respectively, are suppressed, as expected, and found to be compatible with zero.

The $\sin\phi$ amplitude of the beam-helicity asymmetry $A_{LU,\mathrm{I}}$ is shown on the first row of the fig. 19 as a function of $-t$, x_B and Q^2 and in the entire kinematic range. This amplitude exhibits a large overall value with no significant dependence on any of the kinematic variables. As the asymmetry amplitude $A_{LU,\mathrm{I}}^{\sin\phi}$ is expected to vanish in the limit of vanishing $-t$, this implies a rather strong dependence of this amplitude on t for smaller values of $-t$. The $A_{LU,\mathrm{I}}^{\sin\phi}$ amplitude is sensitive to the imaginary part of the CFF $\mathcal{H}$ and thereby can constrain the GPD H. The asymmetry amplitude $A_{LU,\mathrm{DVCS}}^{\sin\phi}$, amplitude of the beam-helicity asymmetry sensitive to the squared DVCS term, and the $\sin 2\phi$ amplitude of $A_{LU,\mathrm{I}}$ are shown in the second and third rows, respectively. They show no kinematic dependence, with overall values compatible with zero, and neither asymmetry amplitude shows any dependence in $-t$, x_B or Q^2.

It is interesting to note that the beam-charge $A_C^{\cos\phi}$ and beam-helicity $A_{LU,\mathrm{I}}^{\sin\phi}$ asymmetry amplitudes show a fundamentally different dependence in $-t$, being related to the real and imaginary parts of the same CFFs (see eqs. (29) and (30)).

The curves in figs. 18 and 19 show the results of model calculations at the average kinematic of the data analysis. The solid curves show results of calculations from a global fit [42] of GPDs to experimental data from HERMES (1996-2005) and the collider experiments at HERA. The dashed curves represent the model fit including the

Jefferson Lab Hall-A data [36]. The dash-dotted curves show the result of calculations from a fit to deep-inelastic and elastic scattering data, and DVCS data from Jefferson Lab, based on a quark-diquark model with a Regge-inspired term to determine the t-dependence of the corresponding GPD [59]. It describes the t-projections of the $A_{LU,\mathrm{I}}^{\sin\phi}$ amplitude well, but the projections in the other kinematic variables are not as well described. The model describes the trends of the beam-charge asymmetry amplitudes $A_C^{\cos(0\phi)}$ and $A_C^{\cos\phi}$ well.

The data used in this analysis were collected without the detection of the recoil nucleon. For the selection of the BH/DVCS processes, it was required that the events contain exactly one charged track identified as a lepton with the same charge as the beam lepton, and one photon being detected in the electromagnetic calorimeter [61]. For this data, events were selected by requiring that the squared missing-mass $M_X^2 = (q + P_N - q')^2$ of the $ep \to e\gamma X$ reaction corresponded to the squared nucleon mass M_N^2, where $P_N = (M_N, 0, 0, 0)$.

Such an event sample includes not only $ep \to ep\gamma$ events but also contamination from the semi-inclusive production of neutral mesons, mostly π^0, where either only one decay photon is detected or the decay photons cannot be resolved (see the left panel of fig. 20). The exclusive region is defined in a mass window to minimize background from deep-inelastic scattering fragmentation processes, while maintaining reasonable efficiency.

The other source of contamination is the "associated" production, where the nucleon is excited to a resonant
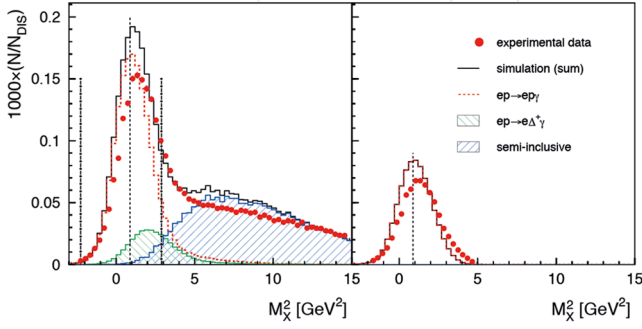
Fig. 20. The distribution in squared missing-mass from data for pre-recoil data (left) and recoil data (right) compared to Monte Carlo simulations (solid line). The latter include the elastic contribution from BH process, $ep \to ep\gamma$, shown as a dashed histogram, as well as the contributions from associated production, $ep \to e\Delta^+\gamma$, and semi-inclusive background shown as hatched histograms. Figure is from ref. [62].

state, $ep \to e\Delta^+\gamma$. This contamination remained part of the signal. The bottom rows of figs. 18 and 19 show the estimated fractional contribution from associated BH production in each kinematic bin. On average it is about 12% within the exclusive region rising with increasing values of $-t$.

6.2 Beam-helicity asymmetry with kinematically complete event reconstruction at HERMES

For the last two years of the data taking, HERMES ran with a recoil detector [63] installed in the target region. The main purpose of this detector was the detection of the recoil target proton in order to enhance access to hard exclusive processes at HERMES, in particular to DVCS.

For the data sample with the recoil detector, a "pure" exclusive event sample is selected by combining information from the recoil detector and forward spectrometer in a kinematic event fit. This fit is based on four-momentum conservation under the hypothesis of the process $ep \to ep\gamma$. It is performed for every exclusive-event candidate by using the three-momenta of the positron and photon measured in the forward spectrometer and the proton candidate in the recoil detector. For more details see ref. [62]. This event selection results in suppression of background contaminations from associated and semi-inclusive processes to a negligible level (less than 0.2%, see the right panel of fig. 20) while keeping the efficiency high ($\approx 83\%$).

The data was recorded with one beam charge only. The real-photon production cross section for an unpolarized target is given as

$$\sigma(\phi, P_\ell, e_\ell) = \sigma_{UU}(\phi) \times [1 + P_\ell A_{LU}(\phi, e_\ell)]. \quad (62)$$

For the definition of the asymmetry A_{LU} see eq. (35). The Fourier amplitudes of the single-charge beam-helicity asymmetry,

$$A_{LU}(\phi, e_\ell) = A_{LU}^{\sin\phi} \sin\phi + A_{LU}^{\sin(2\phi)} \sin(2\phi), \quad (63)$$
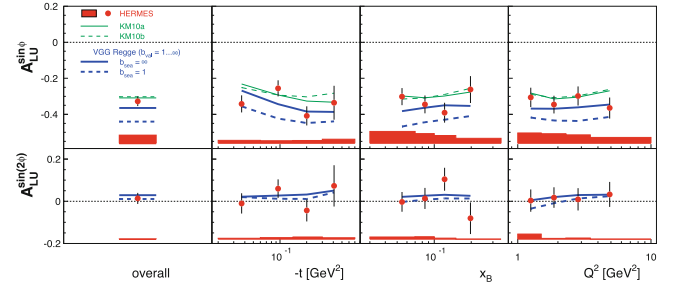
Fig. 21. Amplitudes of single-charge beam-helicity asymmetry extracted from the pure $ep \to ep\gamma$ sample obtained with recoil-proton reconstruction. The amplitudes are presented in projections of $-t$, x_B, and Q^2. The overall results are extracted in a single kinematic bin covering the entire kinematic acceptance. Statistical (systematic) uncertainties are represented by error bars (bands). A separate scale uncertainty arising from the measurement of the beam polarization amounts to 1.96%. The theoretical models are evaluated at the average values of the kinematics and are based on ref. [47] labeled as "VGG Regge" and on ref. [42] labeled as "KM". The figure is from ref. [62].

were extracted [62]. For data collected with only one beam charge, the two terms containing s_1^{DVCS} and s_1^{I} cannot be disentangled. However, at HERMES kinematic conditions, the asymmetry is expected to be dominated by the term containing s_1^{I}. Note that $A_{LU}^{\sin\phi}$ is related, but not identical to s_1^{I} since there is a ϕ-dependence in the denominator. The statement also holds for $A_{LU}^{\sin(2\phi)}$. As a consistency check for extraneous harmonics caused by the ϕ-dependence of the denominator and as a test of the normalization of the fit, the maximum likelihood fit was repeated including the terms $A_{LU}^{\cos(0\phi)}$ and $A_{LU}^{\cos\phi}$. As expected, these spurious terms were found to be compatible with zero within statistical uncertainties and have negligible impact on the resulting asymmetry amplitudes.

The overall value of the leading $\sin\phi$ amplitude at $\langle -t \rangle = 0.13\,\mathrm{GeV}^2$, $\langle x_B \rangle 0.10$ $\langle Q^2 \rangle = 2.63\,\mathrm{GeV}^2$ is negative and significantly different from zero (see fig. 21). Its one-dimensional projections in x_B and Q^2 reveal no dependencies. There is no clear indication for a dependence on $-t$, although this amplitude is expected to approach zero as $-t$ approaches zero. The magnitude for the overall asymmetry amplitude $A_{LU}^{\sin\phi}$ is slightly larger compared to the $A_{LU,\mathrm{I}}^{\sin\phi}$ (see fig. 42). Neglecting the contribution from the squared-DVCS term, this difference arises from the different acceptance of the recoil detector as well as from the elimination of background from associated production.

The overall value of the sub-leading $\sin(2\phi)$ amplitude is compatible with zero within its total experimental uncertainty.

The accuracy of the measurements allows for a rejection of certain GPD models and their parameters. The asymmetry amplitudes are compared with model calculations labeled "VGG Regge" [47]. Variants of this model differ in the t-dependence of GPD H. The skewness dependence is controlled by the b parameter, where b_{val} (b_{sea}) is
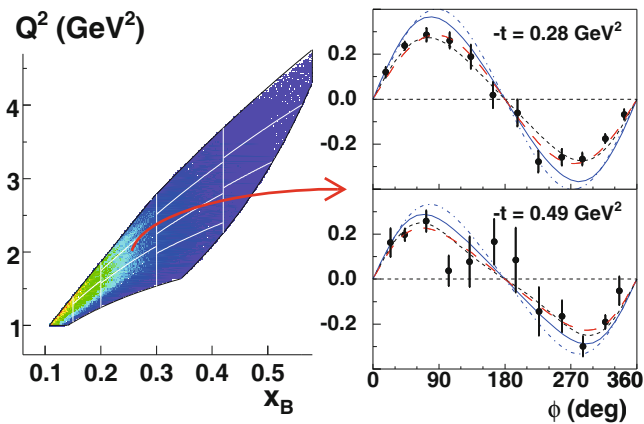
a free parameter for the valence (sea) quarks. The result of the model calculation depends only very weakly on the value of b_{val}. For the sea quarks, the skewness-independent variant of the model ($b_{sea} = \inf$) is consistent with the data, while a maximal skewness dependence ($b_{sea} = 1$) is disfavored.

The other model calculations [42] labeled "KM" is already discussed in the scope of beam-charge and beam-helicity amplitudes. This model calculations agree well with the extracted leading amplitude.
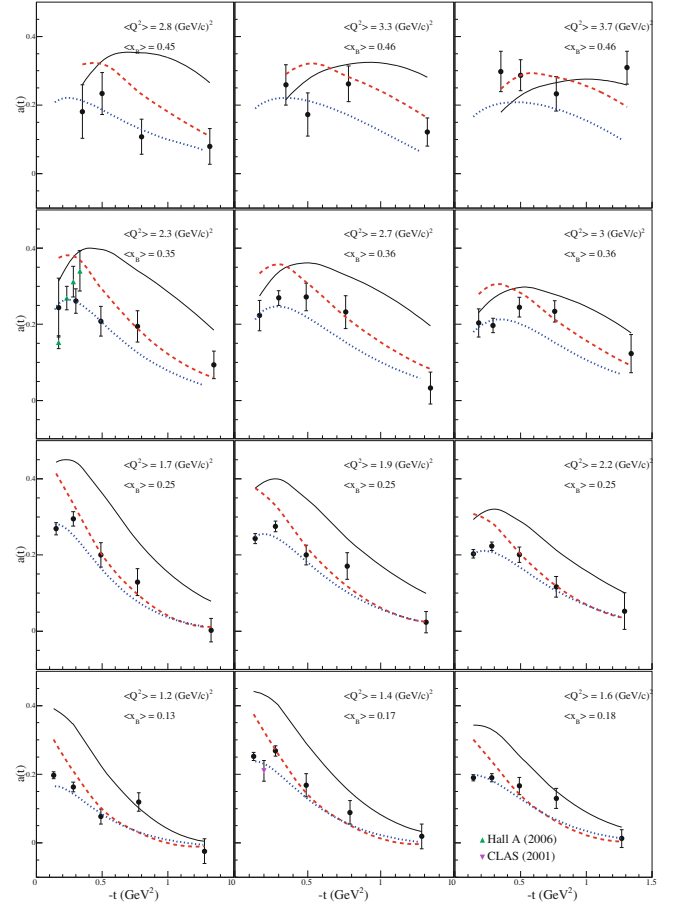
As for the associated processes that remain part of the signal in DVCS analyses for pre-recoil data, HERMES measured the beam-helicity asymmetry in associated electroproduction of real photons, $ep \rightarrow e\gamma\pi N$ in the $\Delta(1232)$-resonance region using the data collected with the recoil detector, longitudinally polarized positron beam and an unpolarized hydrogen target [64]. Azimuthal Fourier amplitudes of this asymmetry are extracted separately for two channels, $ep \rightarrow e\gamma\pi^0 p$ and $ep \rightarrow e\gamma\pi^+ n$. All asymmetry amplitudes are found to be consistent with zero.

6.3 Beam-spin asymmetries from CLAS

The data were taken during the E01-113 experiment, described in sect. 5.3. After detecting $ep\gamma$ events and applying the standard CLAS fiducial cuts to exclude the least efficient areas of the detector, kinematic cuts were applied in order to ensure exclusivity. The remaining background, due to the $ep\pi^0$ events where only one of the two decay photons was detected which survived the exclusivity cuts, was estimated, using Monte-Carlo simulations and detected $ep\pi^0 \rightarrow e'p'\gamma\gamma$ events, and subtracted [52]. In order to extract beam-spin asymmetries, the selected data sample was divided into 12 bins in the (Q^2, x_B) plane (fig. 22,

Fig. 23. $a = A_{LU}(90°)$ as a function of $-t$, where A_{LU} is the DVCS beam-spin asymmetry extracted with CLAS [52]. Each individual plot corresponds to a bin in (x_B, Q^2). The experimental points (black circles) are compared to previous results from ref. [26] (purple upside-down triangles) or extracted from cross section measurements [36] (green triangles), at similar — but not equal— values of $\langle x_B \rangle$ and $\langle Q^2 \rangle$. The curves are the following GPD model predictions: VGG [11, 28, 45, 47] (blue dotted line), GK [66–68] (solid black line), and KM15 [69] (red dashed line).
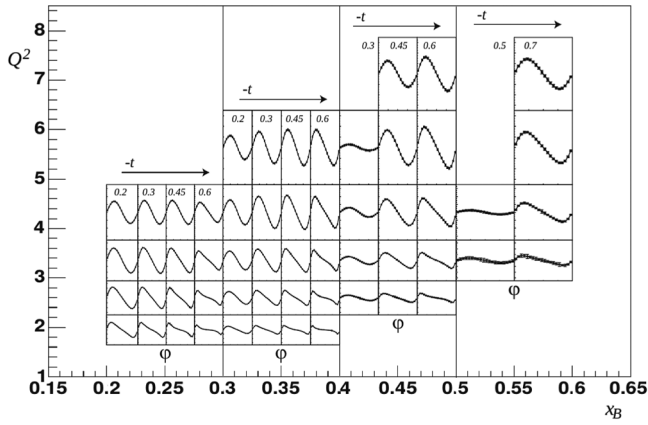
left), in 5 bins in $-t$ (from $0.09\,\mathrm{GeV}^2$ up to $1.8\,\mathrm{GeV}^2$), and in 12 bins in ϕ, each $30°$ wide [52]. For each bin in Q^2, x_B and t the asymmetry was fitted according to the leading-twist expansion of eq. (35), neglecting higher-twist terms and retaining only dominant terms, with the function

$$A = \frac{a \sin \phi}{1 + c \cos \phi}, \qquad (64)$$

where the $\cos 2\phi$ term of the denominator was omitted, since its contribution was found to be consistent with zero [52]. The fit is represented by the red long-dashed curve in fig. 22, right side. The parameter a, corresponding to the asymmetry at $90°$, appears to be dominant with respect to c at the lowest $-t$ values. Its evolution as a function of $-t$ for each (Q^2, x_B) is plotted in fig. 23.

The obtained values of $a(t)$, which are in good agreement with the previous CLAS result [26] and with the

Fig. 22. Left: kinematic coverage and binning in the (Q^2, x_B) plane. Right: beam-spin asymmetry as a function of ϕ for 2 of the 57 (Q^2, x_B, t) bins. The red long-dashed curve corresponds to the fit with eq. (64), without the term in $\cos 2\phi$. The (black) dashed curve is a Regge calculation [65]. The other blue curves correspond to the GPD calculation of ref. [45] at twist-2 (solid) and twist-3 (dot-dashed) levels [29], with the contribution of the GPD H only. This figure is from ref. [52].
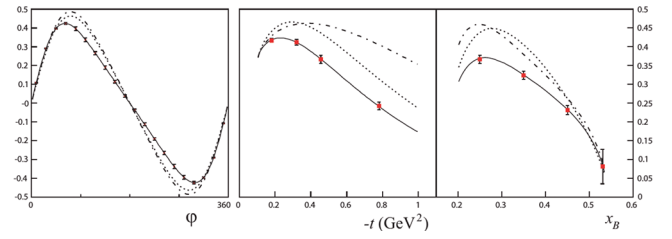
Fig. 24. Expected statistical accuracy and kinematical coverage for the beam-spin asymmetry that will be measured with CLAS12, as a function of $(x_B, Q^2, -t)$. The outer x-axis corresponds to the x_B range, divided into 4 bins. The outer y-axis represents the Q^2 range. Each individual histogram is the BSA (plotted between -0.7 and 0.7) as a function of ϕ (between 0 and 2π) for a given $-t$ bin. The average value of $-t$ in the bin is shown in the upper part of each histogram. Figure taken from ref. [70].

Fig. 25. The red points are, for all three figures, the projected beam-spin asymmetries that will be measured in the upcoming CLAS12 experiment. Left: BSA as a function of ϕ, for $\langle x_B \rangle = 0.2$, $\langle Q^2 \rangle = 3.3\,\mathrm{GeV^2}$, $\langle -t \rangle = 0.45\,\mathrm{GeV^2}$. Middle: BSA as a function of $-t$, for $\langle x_B \rangle = 0.2$, $\langle Q^2 \rangle = 3.3\,\mathrm{GeV^2}$, $\langle \phi \rangle = 90°\,\mathrm{GeV^2}$. Right: BSA as a function of x_B, for $\langle -t \rangle = 0.45$, $\langle Q^2 \rangle = 3.3\,\mathrm{GeV^2}$, $\langle \phi \rangle = 90°\,\mathrm{GeV^2}$. The lines are the predictions of the VGG model, with different options: Regge-like t-dependence and inclusion of the "D-term" (solid line); Regge-like t-dependence without D-term (dotted line); t-dependence from the electromagnetic form factors, D-term included (dash-dotted line). Figure taken from ref. [70].

points from Hall A [36], are compared to the predictions of three GPD parametrizations: VGG [11, 28, 45, 47], GK [66–68], and KM15 [69]. Systematic studies on various versions of these two double-distributions based models (VGG and GK) were done in ref. [15], and here only the versions providing the best fits to the data are shown. In the version of the VGG model shown here, the contributions of the GPDs H, $\tilde{H}$, and E were included. For H and E the D-term is also included. The parametrization of E includes both valence- and sea-quarks contributions. The VGG model tends to overestimate the experimental asymmetries at low t, expecially at low values of Q^2 and x_B. The agreement with the data improves as x_B increases. For the GK model, only the contribution from the GPD H was retained here, as the inclusion of other GPDs worsened the agreement with the data. GK systematically overestimates the experimental asymmetry amplitude, especially at low $-t$, and, similarly as for VGG, has a slightly better agreement in the high-Q^2 region. The best fit to the data is provided by the KM15 model, which is expected since these data are included in the fit of the model parameters. It must be noted that for $-t > Q^2/4$ the KM15 model lines are just a naive extrapolation, and any partonic interpretation (*e.g.* for 3D imaging) is not justified.

6.4 Beam-spin asymmetry measurements with CLAS12

With its large acceptance, good particle identification capability and high luminosity ($L \simeq 10^{35}\,\mathrm{cm^{-2}\,s^{-1}}$, a factor of 10 more than the old CLAS), the upgraded CLAS12 will be very well suited to study nucleon structure at high x_B. The experimental program for the first 5 years of operation of CLAS12 will be mainly focused on measurements

of GPDs in exclusive processes. In particular, the first experiment to run will be mainly geared towards the extraction of beam-spin asymmetries for the $\vec{e}p \to ep\gamma$ reaction. Similarly to what was done for the 6 GeV DVCS experiments in CLAS, the $ep\gamma$ final state will be fully detected. Figure 24 shows the expected coverage and statistical accuracy for the projected BSA, that will be obtained for 80 days of running. The relative systematic uncertainties will not exceed 5%.

The precision and kinematical coverage of these asymmetries will bring stringent constraints to GPD parametrizations, as can be seen in fig. 25. With such a wide t and Q^2 coverage, it will be possible to study the onset of twist-3 effects or higher, which enter the BSA as powers of $\sqrt{-t}/Q$. Furthermore these BSAs, combined to the other proton-DVCS observables that will be measured with CLAS12 (sects. 7.3, 8.2), will contribute to the extraction, via global fit of parametrized GPDs or via model-independent local fits, of the CFFs of the proton.

The measurement of the $\vec{e}p \to ep\gamma$ absolute cross sections and cross section differences will be another objective of this experiment. In this case, the relative systematic uncertainties, expected to be at the 10% level, will dominate over the statistical ones.

7 DVCS on longitudinally polarized target

In case of longitudinally polarized target, the asymmetries appearing in the distribution of the real photons in the azimuthal angle ϕ,

$$\sigma(\phi, e_\ell, P_\ell, S_L) = \sigma_{UU}(\phi, e_\ell)\{1 + S_L\, A_{UL}(\phi) + P_\ell\, S_L\, A_{LL}(\phi) + P_\ell\, A_{LU}(\phi)\}, \quad (65)$$

are the target single-spin A_{UL} and double-spin A_{LL} asymmetries defined in eqs. (39) and (46). Both the HERMES and the CLAS Collaboration produced results on both of

these observables, and they are shown in the following sections. The longitudinally polarized hydrogen data at HERMES and CLAS were taken solely with one lepton-beam charge (positron for HERMES, electron for CLAS). Thus, the direct separation of the squared-DVCS and interference terms is not possible.

7.1 HERMES results

In the analysis of HERMES data, the asymmetries for longitudinally polarized target were decomposed as

$$A_{UL}(\phi) \simeq \sum_{n=1}^{3} A_{UL}^{\sin(n\phi)} \sin(n\phi), \qquad (66)$$

$$A_{LL}(\phi) \simeq \sum_{n=0}^{2} A_{LL}^{\cos(n\phi)} \cos(n\phi). \qquad (67)$$

The $A_{UL}^{\sin\phi}$ and $A_{LL}^{\cos\phi}$ asymmetry amplitudes receive leading-twist contributions via the Fourier coefficients $s_{1,LP}^{I}$ and $c_{1,LP}^{I}$, respectively and twist-3 contribution from $d\sigma_{UL}^{DVCS}$ and $d\sigma_{LL}^{DVCS}$ (see eqs. (39) and (46)). The dominance of the interference term over the squared-DVCS term, combined with the additional $\frac{1}{Q}$-suppression arising from the twist-3 nature of the squared-DVCS contribution, makes $A_{UL}^{\sin\phi}$ and $A_{LL}^{\cos\phi}$ the simplest of the asymmetry amplitudes in this series of asymmetries from which the GPD-related information can be extracted. More specifically, it is expected that these measurements can be used to constrain the values of the CFF $\widetilde{\mathcal{H}}$. The $A_{UL}^{\sin\phi}$ amplitude is sensitive to the imaginary part of the CFF $\widetilde{\mathcal{H}}$, whereas the $A_{LL}^{\cos\phi}$ amplitude is sensitive to the real part of the same CFF (see eqs. (40) and (47)).

The $A_{LL}^{\cos 0\phi}$ asymmetry amplitudes receives leading-twist contributions from interference and pure DVCS coefficients, $c_{0,LP}^{I}$ and $c_{0,LP}^{DVCS}$, and also an additional contribution from BH coefficients $c_{0,LP}^{BH}$. The tangled mix of contributions to these amplitudes increases the difficulty of extracting information related to CFFs and therefore GPDs from it.

The higher-order Fourier components of the asymmetries of eqs. (66) and (67) receive twist-3 or gluon-transversity contributions.

Figures 26 and 27 respectively show the asymmetry amplitudes $A_{UL}^{\sin(n\phi)}$ and $A_{LL}^{\cos(n\phi)}$ integrated over the HERMES acceptance ("integrated") as well as projected across the kinematic variables $-t$, x_B and Q^2. The first harmonic of the A_{UL}, when extracted in the entire kinematic range ($\langle -t \rangle = 0.12\,\text{GeV}^2$, $x_B = 0.10$, $\langle Q^2 \rangle = 2.46\,\text{GeV}^2$), exhibits the value $-0.073 \pm 0.032(\text{stat.}) \pm 0.007(\text{syst.})$. The $A_{UL}^{\sin(2\phi)}$ amplitude has an unexpectedly large value when extracted from the integrated kinematic range of the data set. This asymmetry amplitude is expected to receive a mixture of quark twist-3 and gluon twist-2 CFF contributions, and as such could have been expected to be small in
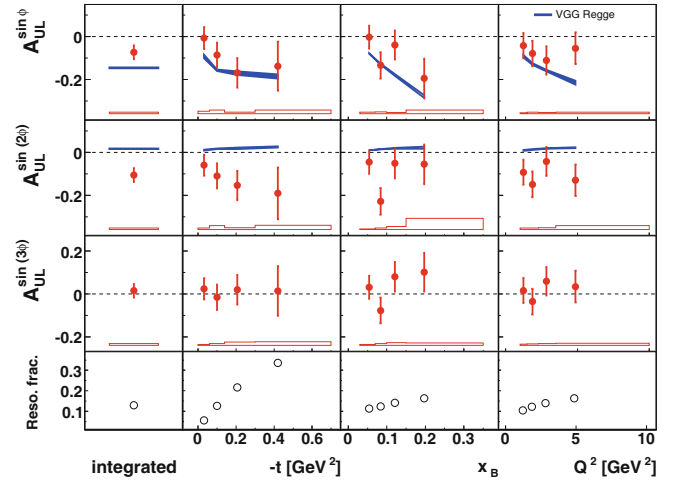
Fig. 26. Amplitudes of the target single-spin asymmetry A_{UL} extracted in the entire kinematic range, as well as a function of $-t$, x_B, and Q^2. The error bars (open red bands) show the statistical (systematic) uncertainties and the solid blue bands represent the predictions from the "VGG Regge" GPD model described in ref. [47]. The fractional contributions from resonance production estimated from an MC model are presented in the bottom panel. This figure is from ref. [71].
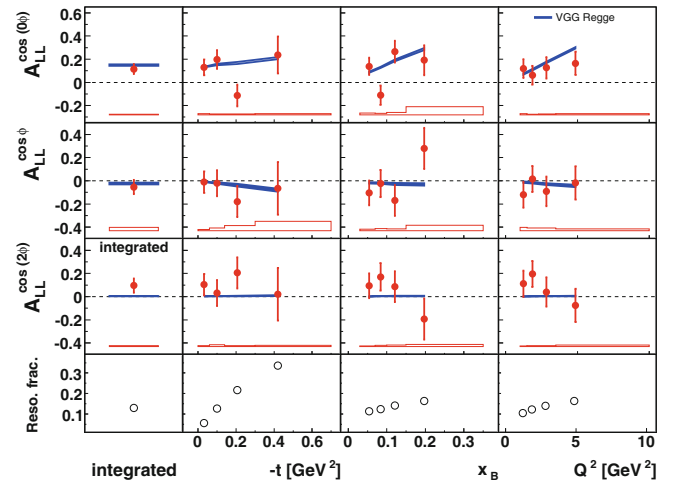
Fig. 27. Amplitudes of the target double-spin asymmetry A_{LL} extracted in the entire kinematic range, as well as a function of $-t$, x_B, and Q^2. The error bars (open red bands) show the statistical (systematic) uncertainties and the solid blue bands represent the predictions from the "VGG Regge" GPD model described in ref. [47]. The fractional contributions from resonance production estimated from an MC model are presented in the bottom panel. Figure taken from ref. [71].

the HERMES kinematic range. The kinematic projections provide no evidence of strong dependences on $-t$, x_B, or Q^2 for either of the asymmetry amplitudes. The $A_{UL}^{\sin(3\phi)}$ amplitude is found to be consistent with zero.

The dominating contribution for the double-spin asymmetry $A_{LL}^{\cos(0\phi)}$ is from the Bethe-Heitler Fourier coefficient $c_{0,LP}^{BH}$. It is therefore expected to be positive and non-zero, as confirmed by the data. No dependences are

observed in the data across projections $-t$, x_B, and Q^2. The other two harmonics of the double-spin asymmetry $A_{LL}^{\cos\phi}$ and $A_{LL}^{\cos(2\phi)}$ are compatible with zero.

All asymmetry amplitudes are presented in comparison with calculations [47], labelled "VGG Regge". Predictions from this model have been compared previously with HERMES results with respect to beam-helicity and beam-charge asymmetries. This is the same model that failed to predict the HERMES results for the beam-helicity asymmetry [60].

The amplitude $A_{UL}^{\sin\phi}$ is well described by the model, which predicts the kinematic trend and the magnitude of this amplitude with reasonable accuracy. However, the relatively large amplitude $A_{UL}^{\sin(2\phi)}$ is not described by the model, which predicts that the amplitude should be small and of opposite sign.

Figure 27 shows that the predictions made by the model of the A_{LL} asymmetry mostly agree with the data both regarding the magnitude and trends of the amplitudes. It describes the positive, slightly increasing trend for the $A_{LL}^{\cos(0\phi)}$ amplitude observed in the data across all three variables. The prediction of the model for values of the $A_{LL}^{\cos\phi}$ and $A_{LL}^{\cos(2\phi)}$ is compatible with the data within the uncertainties of the extraction.

The fractional contribution of the resonant state production (*i.e.* "Reso. frac.") to the data set is estimated from MC simulations and shown in the bottom rows of figs. 26 and 27.

7.2 CLAS results

The data, part of the E05-114 experiment which ran in Hall B at Jefferson Lab during the year 2009, were produced by a roughly 5.9 GeV polarized electron beam impinging onto a solid ammonia target (NH_3), polarized along the beam direction [72], and collected by the CLAS detector. Exclusive $ep\gamma$ events were extracted, applying cuts on missing masses and angles formed with the quadrivectors of the detected electron, proton, and photon. These cuts served the dual purpose of suppressing the background of events scattered from the nuclear target (N_{14}) and the $ep\pi^0$ events, with only one decay photon reconstructed, mimicking the $ep\gamma$ final state. The phase space covered by the selected events was divided into 21 bins in (Q^2, x_B, $-t$).

For each (Q^2, x_B, $-t$) bin, beam, target, and double-spin asymmetries were extracted as a function of ϕ, in ten equidistant bins (see the example of the target-spin asymmetry in fig. 28). The two single-spin asymmetries were fitted with the function

$$\frac{\alpha_{LU(UL)}\sin\phi}{1+\beta\cos\phi},\qquad(68)$$

according to the leading-twist harmonic expansion of eq. (39). The left plot of fig. 29 shows the parameter α for the TSA, *i.e.* its value at $\phi = 90°$, as a function of $-t$, for the five measured $Q^2 - x_B$ bins, compared to four GPD
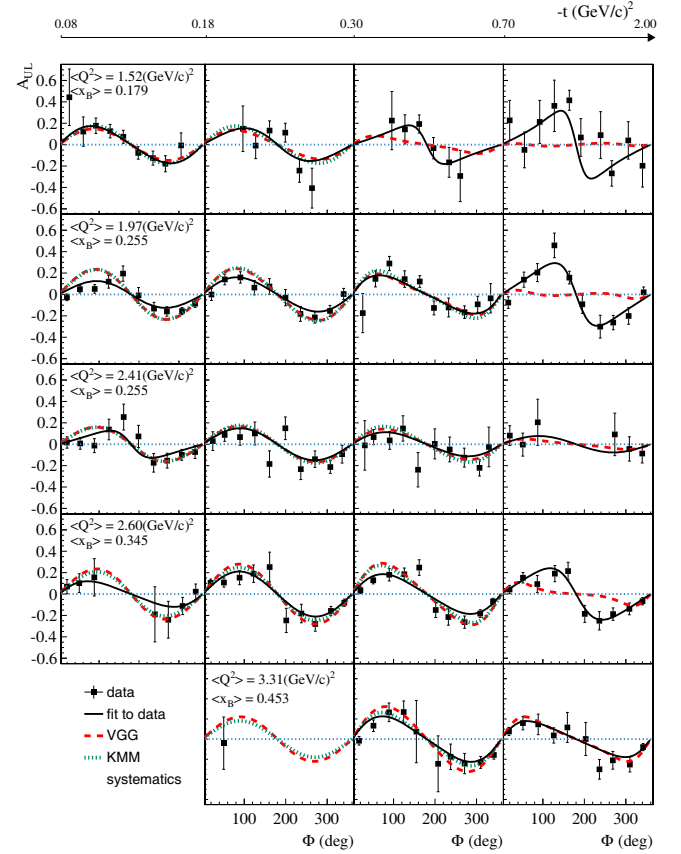
Fig. 28. Longitudinal target-spin asymmetry for the reaction $ep \to e'p'\gamma$ as a function of ϕ, for the 19 (Q^2, x_B, $-t$) bins. The point-by-point systematic uncertainties are represented by the shaded bands. The solid black curve is the fit with the function $\frac{\alpha_{UL}\sin\phi}{1+\beta\cos\phi}$. The curves show the predictions of the VGG [28,47] (red-dashed) and KMM12 [73] (green-dotted) models. Figure taken from ref. [74].

models, described in the caption. The amplitude of the target-spin asymmetry seems rather constant as a function of all kinematic variables, $-t$ included, apart from the expected systematic drop towards $t \sim t_{min}$. This trend is quite different from what is observed for the beam-spin asymmetry, which is found to be consistent with the one previously measured at CLAS [52], which displays a much stronger drop, by about a factor of 3 on average, for all Q^2-x_B kinematics but more markedly at low x_B. As mentioned in sect. 2 the DVCS/BH beam-spin and target-spin asymmetries are mostly sensitive to the GPDs H and to a combination of $\tilde{H}$ and H, respectively. Therefore, considering that the t-slope of the GPDs is linked via a Fourier transform to the transverse position of the struck parton [8], this result suggests that the axial charge (linked to $\Im m\tilde{\mathcal{H}}$) is more concentrated in the center of the nucleon than the electric charge (linked to $\Im m\mathcal{H}$), confirming what was first observed in [75]. This is in agreement with the behavior as a function of Q^2 of the axial form factor, which is the first moment in x of $\tilde{H}$, and which was measured in π^+ electroproduction experiments on the proton as well as in neutrino-nucleon scattering [76]. These results adds to
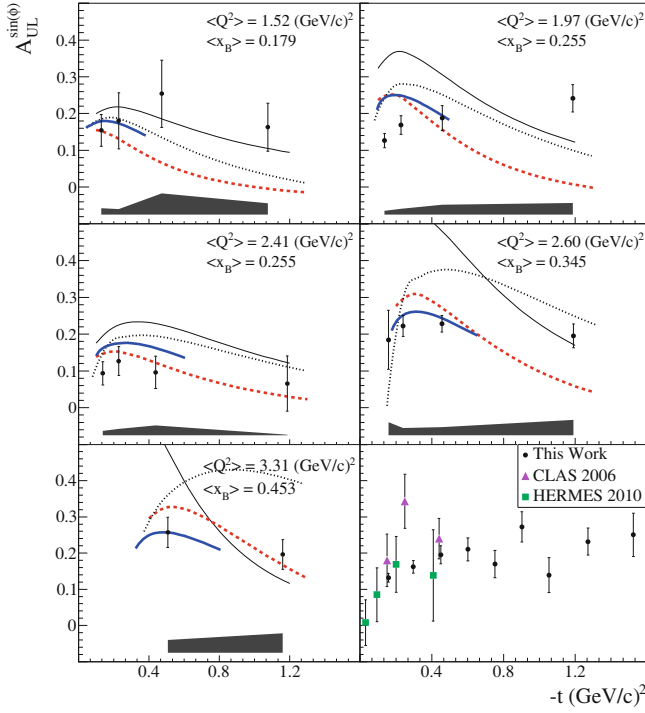
Fig. 29. First five plots: $-t$-dependence of the $\sin\phi$ amplitude of A_{UL} for each Q^2-x_B bin. The shaded bands represent the systematic uncertainties. The curves show the predictions of four GPD models: i) VGG [28, 47] (red-dashed), ii) KMS12 [48] (black-dotted), KMM12 [73] (blue-thick solid), GGL [59, 77] (black-solid). Bottom right plot: comparison of the $\sin\phi$ amplitude of A_{UL} as a function of $-t$ for the results of this work (black dots) integrated over all Q^2 and x_B values ($\langle Q^2 \rangle = 2.4\,\text{GeV}^2$, $\langle x_B \rangle = 0.31$), the HERMES results [78] (green squares) at $\langle Q^2 \rangle = 2.459\,\text{GeV}^2$, $\langle x_B \rangle = 0.096$, and the previously published CLAS results [79] (pink triangles), at $\langle Q^2 \rangle = 1.82\,\text{GeV}^2$, $\langle x_B \rangle = 0.28$. The figure is from ref. [80].

this the extra information on the longitudinal momentum of the partons.

Aside from the highest-x_B point, in which VGG reproduces well the data, the flat $-t$ slope of the target-spin asymmetry is clearly not predicted by the VGG or KMS12 models, which instead display a similar drop with t for the TSA as what was computed for the BSA. These models approximately reproduce the low-t magnitude of the asymmetry in some kinematics, with a slightly better fit of the data for VGG. KMS12 predicts an increase of the TSA with x_B that is not observed in the experiment. The GGL model also predicts a drop in $-t$ not confirmed by the data, and moreover it overestimates the magnitude of the asymmetry by at least a factor of 2. The best fit to the data is provided, in the bins where it applies, by the KMM12 model.

The double-spin asymmetry, which appears, with respect to the single-spin asymmetry, rather flat in ϕ and of larger magnitude (~ 0.6), was fitted with the $\frac{\kappa_{LL} + \lambda_{LL}\cos\phi}{1 + \beta\cos\phi}$ function. The constant term, κ_{LL}, which is found to dominate the asymmetry, is shown, as a function of $-t$ and
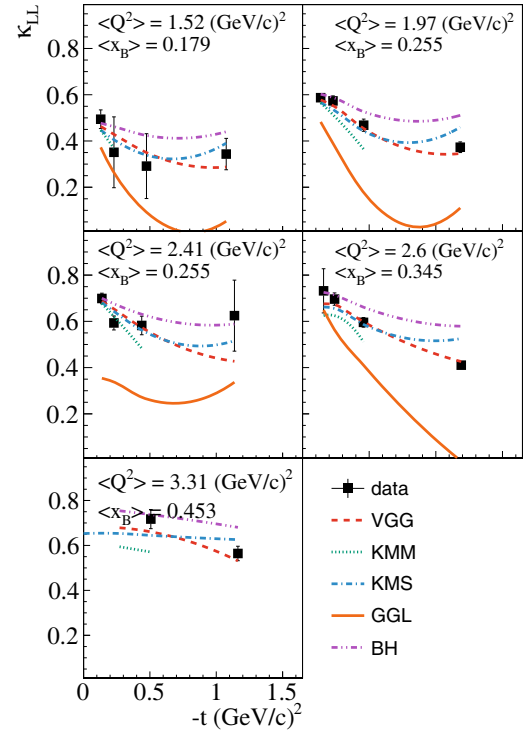
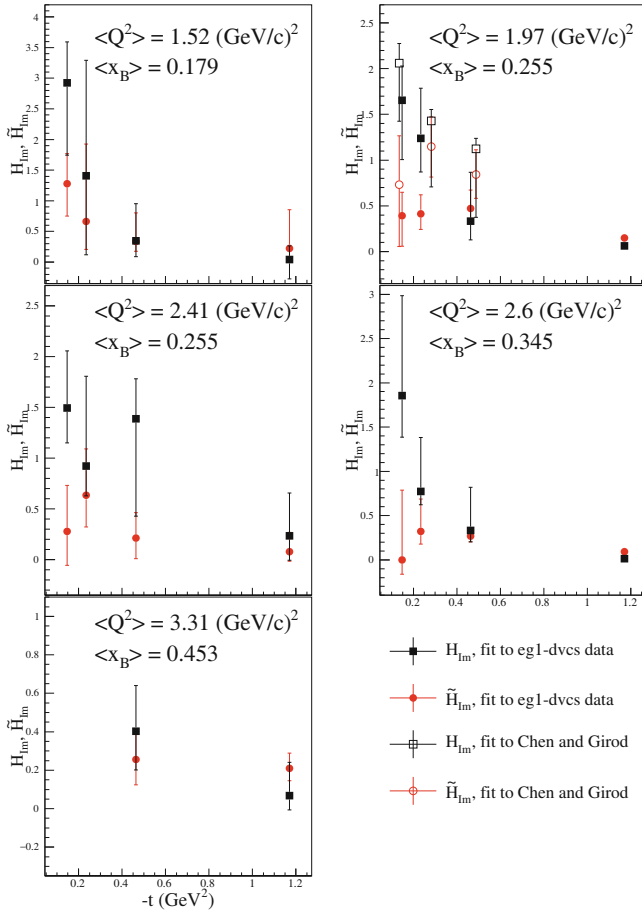**Fig. 30.** $-t$-dependence, for each Q^2-x_B bin, of the constant term κ_{LL} (right) of the double-spin asymmetry. The pink two-dot-dashed curves are the calculations of the DSA for the BH process alone. The curves show the predictions of four GPD models for the TSA at $\phi = 90°$: i) VGG [28, 47] (red dashed), ii) KMM12 [73] (green dotted), iii) KMS12 [48] (blue dash-dotted), and iv) GGL [59, 77] (orange dash-triple-dotted). The figure is from ref. [74].

for each Q^2-x_B bin in fig. 30. It appears that BH fully accounts for the constant term, and all models —except for GGL, which misses both the magnitude and the t-dependence of this observable— predict this and correctly reproduce it. The models tend to suggest a slight contribution from DVCS in the $\cos\phi$ term but the statistical precision of the data does not allow one to draw definitive conclusions on this.

The three sets of asymmetries (BSA, TSA and DSA) for all kinematic bins were processed using the fitting procedure described in [15, 55] to extract the Compton Form Factors. In the adopted version of the fitter code, seven out of the eight real and imaginary parts of the CFFs are left as free parameters in the fit ($\tilde{E}_{Im} = 0$). Figure 31 shows H_{Im} (black full squares) and $\tilde{H}_{Im}$ (red full circles), which are obtained from the fit of the CLAS E05-114 data, as a function of $-t$ for each of the 5 Q^2-x_B bins. These are the two CFFs that appear to be better constrained by these results. Given that the size of the error bars reflects the sensitivity of the combination of observables to each CFF, it is evident that, as expected, these asymmetries are mostly sensitive to $\Im m\tilde{\mathcal{H}}$.

The results for H_{Im} and $\tilde{H}_{Im}$ confirm what had been previously observed in a qualitative way by direct comparison of the t-dependence of TSAs and BSAs: the t-slope

Fig. 31. $-t$-dependence for each Q^2-x_B bin of H_{Im} (black squares) and $\tilde{H}_{Im}$ (red circles). The full points are obtained by fitting the E05-114 data (TSA, BSA and DSA) [74]. The empty points were obtained by fitting the BSA results from [52] integrated over all values of Q^2 at $x_B \sim 0.25$, and the TSAs from [79]. Figure taken from ref. [74].

of $\Im m\mathcal{H}$ is much steeper than that of $\Im m\tilde{\mathcal{H}}$, hinting that the axial charge (linked to $\Im m\tilde{\mathcal{H}}$) might be more "concentrated" in the center of the nucleon than the electric charge (linked to $\Im m\mathcal{H}$). This effect seems stronger at the lowest values of x_B, while both CFFs tend to flatten out as x_B increases.

It is also interesting to compare the results obtained for the two equal-x_B bins ($Q^2 = 1.97\,\text{GeV}^2$ and $Q^2 = 2.41\,\text{GeV}^2$): within the limits imposed by the size of the error bars and by the Q^2 lever arm (only $0.44\,\text{GeV}^2$), both sets of CFFs are compatible, at the $1\,\sigma$ level, which supports the validity of the scaling hypothesis.

In fig. 31 the values of H_{Im} and $\tilde{H}_{Im}$ that were obtained [75] using the same fitting code with the results from E01-113 [52] for the beam-spin asymmetry and from a previous polarized-target CLAS experiment [79] for the target-spin asymmetry, are also shown. Aside from the much larger kinematic coverage for the polarized-target observables made accessible by the new data, in the kinematics where the previous extraction had been attempted, they improve the precision of $\Im m\tilde{\mathcal{H}}$.
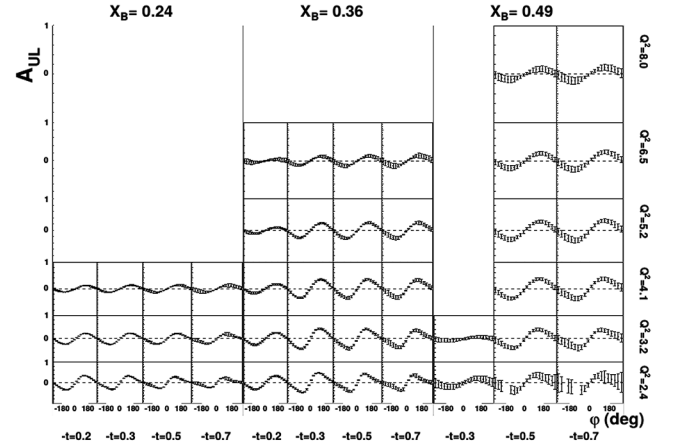
Fig. 32. Projections for the CLAS12 target-spin asymmetry *versus* ϕ, for different Q^2, x_B, and $-t$ values (see caption of fig. 24 for the explanation of the axes). The error bars are statistical. Figure taken from ref. [70].
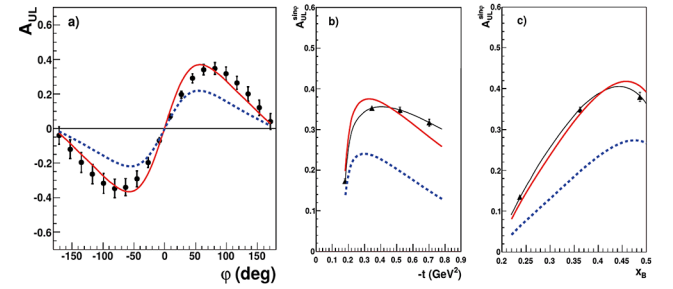
Fig. 33. (a) Target-spin asymmetry as a function of ϕ for $Q^2 = 4.1\,\text{GeV}^2$, $x_B = 0.36$, and $-t = 0.52\,\text{GeV}^2$. (b), (c) $\sin\phi$ moments of the TSA respectively *versus* $-t$ at $Q^2 = 4.1\,\text{GeV}^2$, $x_B = 0.36$, and *versus* x_B at $Q^2 = 4.1\,\text{GeV}^2$, $-t = 0.52\,\text{GeV}^2$. The black points show values obtained with a version of the VGG model [47] that used CTEQ6 PDFs, and the error bars show the statistical procision expected for the CLAS12 experiment. The red solid and the blue dashed curves are also predictions of the VGG model with MRST02 PDFs and, respectively, $E = \tilde{E} = 0$, and $\tilde{H} = E = \tilde{E} = 0$. Figure taken from ref. [70].

7.3 CLAS12 planned experiment

The E05-114 results brought important new information on the x_B- and t-dependence of CFFs, especially $\Im m\tilde{\mathcal{H}}$, on quite a wide kinematical coverage, but their low statistics allowed to perform only a rather coarse four-dimensional binning. This shortcoming will be compensated by the planned CLAS12 experiment for DVCS at $11\,\text{GeV}$ on a longitudinally polarized ammonia target [70]. Figure 32 illustrates the precision and coverage that will be obtained for the target-spin asymmetry, which will permit a precise tuning of GPD parametrizations (fig. 33), in particular for $\tilde{H}$. The double-spin asymmetry A_{LL} will be a by-product of this experiment, bringing sensitivity to the real part of CFFs.

It must be noted that the fact that TSA and DSA will be measured on the same kinematic grid as the BSA (sect. 6.3), will permit to separate the contributions of the $\Im m\mathcal{H}$ and $\Im m\tilde{\mathcal{H}}$ CFFs, as was done in the 6 GeV CLAS experiment (fig. 31).

8 Azimuthal asymmetries on transversely polarized target

In the case of a transversely polarized target, the experimental observables that provide sensitivity to the coefficients appearing in eq. (19), (20), (25) and (26) are the transverse target single-spin A_{UT} and double-spin A_{LT} asymmetries:

$$
\begin{aligned}
\sigma = \sigma_{UU}(\phi)\Big\{ &1 + e_\ell A_C(\phi) + e_\ell P_\ell A_{LU}^{I}(\phi) + P_\ell A_{LU}^{DVCS}(\phi) \\
&+ S_\perp A_{UT}^{DVCS}(\phi, \phi_S) + e_\ell S_\perp A_{UT}^{I}(\phi, \phi_S) \\
&+ P_\ell S_\perp A_{LT}^{BH+DVCS}(\phi, \phi_S) + e_\ell P_\ell S_\perp A_{LT}^{I}(\phi, \phi_S) \Big\}.
\end{aligned}
\tag{69}
$$

For definitions of the asymmetries see eqs. (41), (42) and ref. [25]. The only existing DVCS data, as of today, on transversely polarized protons were produced by the HERMES Collaboration. They will be complemented by CLAS12 data in the near future.

8.1 HERMES results

In the analysis of HERMES data, the A_{UT}^{I} and A_{UT}^{DVCS} asymmetries were expanded in ϕ and $\phi - \phi_S$ as

$$
\begin{aligned}
A_{UT}^{DVCS}(\phi, \phi_S) = &\sum_{n=0}^{3} A_{UT,DVCS}^{\sin(\phi-\phi_S)\cos(n\phi)} \sin(\phi-\phi_S)\cos(n\phi) \\
&+ \sum_{n=1}^{3} A_{UT,DVCS}^{\cos(\phi-\phi_S)\sin(n\phi)} \cos(\phi-\phi_S)\sin(n\phi),
\end{aligned}
\tag{70}
$$

$$
\begin{aligned}
A_{UT}^{I}(\phi, \phi_S) = &\sum_{n=0}^{3} A_{UT,I}^{\sin(\phi-\phi_S)\cos(n\phi)} \sin(\phi-\phi_S)\cos(n\phi) \\
&+ \sum_{n=1}^{3} A_{UT,I}^{\cos(\phi-\phi_S)\sin(n\phi)} \cos(\phi-\phi_S)\sin(n\phi).
\end{aligned}
\tag{71}
$$

As in the unpolarized target case (see sect. 6.1), the separation of the individual terms in eq. (69) is possible combining data collected with both beam charges and helicities on a transversely polarized hydrogen target.

Selected results [81] are presented on fig. 34, in the entire kinematics range ($\langle -t \rangle = 0.12\,\text{GeV}^2$, $x_B = 0.09$, $\langle Q^2 \rangle = 2.5\,\text{GeV}^2$). The amplitudes $A_{UT,DVCS}$ and $A_{UT,I}$ for the same azimuthal dependence are shown together in each panel, even though they typically do not relate to the same GPDs. The filled symbols represent the asymmetry amplitudes related to the coefficients given in
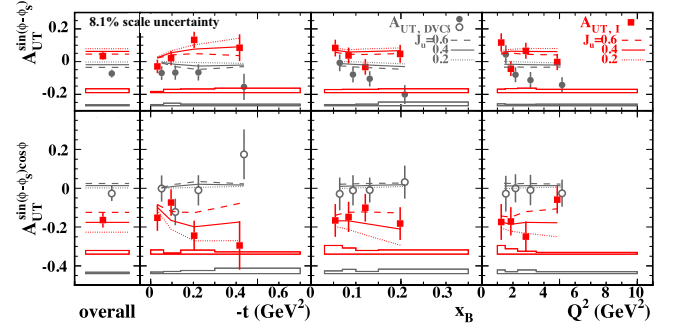
Fig. 34. Asymmetry amplitudes of the squared DVCS amplitude $A_{UT,DVCS}$ (circles) and the interference term $A_{UT,I}$ (squares). The error bars (bands) represent the statistical (systematic) uncertainties, excluding the 8.1% scale uncertainty due to the target polarization measurement uncertainty. The curves are predictions of the VGG model [11, 28, 45, 47], with three different values for the u-quark total angular momentum J_u and fixed d-quark total angular momentum $J_d = 0$ [82]. The figure is from ref. [81].

eqs. (43)–(45). The amplitudes represented by the unfilled symbols are expected to be suppressed, and are indeed found to be typically small.

The amplitudes $A_{UT,I}^{\sin(\phi-\phi_S)\cos(n\phi)}$, $n = 0, 1$ are found to have substantial magnitudes with opposite signs but with little kinematic dependence. Their opposite signs are expected from eq. (44). The overall result of the amplitude $A_{UT,DVCS}^{\sin(\phi-\phi_S)}$, shown in the top row of fig. 34, is non-zero by 2.8 times the total uncertainty. This measurement provides the first experimental evidence for an azimuthal harmonic in the squared DVCS amplitude.

In the particular model calculation [11, 28, 45, 47, 82], assuming the knowledge of the GPDs H, $\tilde{H}$, and $\tilde{E}$, these amplitudes are sensitive to the GPD E. An interesting feature of the VGG model is that the parametrization of the GPD E is dependent on the two parameters J_u and J_d. A given shape in x for the GPD E^q is assumed, and then the overall normalization is proportional to J_q (see ref. [11] for more details). Therefore, in the VGG framework an observable which is sensitive to E provides information on the total angular momenta of the quarks J_q. In fig. 34, the model calculations show relevant sensitivity to J_q. The curves are produced for three different values of $J_u(0.2, 0.4, 0.6)$, while fixing $J_d = 0$. Although this model fails to describe the data for $A_{UT,DVCS}^{\sin(\phi-\phi_S)}$, it confirms that the asymmetry amplitudes have significant sensitivity to J_u.

The amplitude $A_{UT,DVCS}^{\sin(\phi-\phi_S)\cos\phi}$ is expected to be suppressed, and is indeed found to be small.

The double-spin asymmetries A_{LT}^{I} and $A_{LT}^{BH+DVCS}$ are related to the real part of the same combination of CFFs as that determining the transverse target single-spin asymmetries through the imaginary part (see sects. 2.6 and 2.7). The results [25] for the leading Fourier amplitudes of beam-charge-difference asymmetry A_{LT}^{I} are shown in fig. 35. The results for various harmonics of the
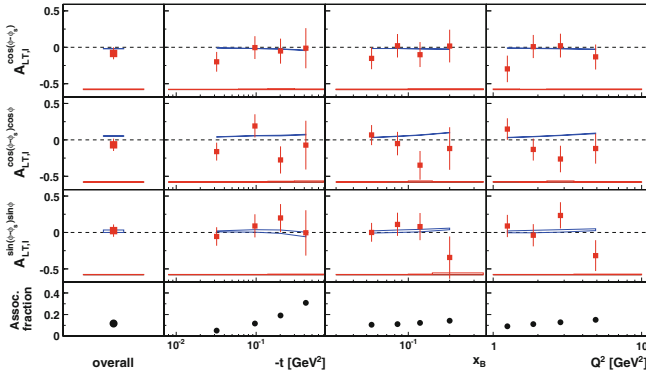
Fig. 35. Charge-difference double-spin asymmetry amplitudes describing the dependence of the interference term on transverse target polarization in combination with beam helicity and beam charge extracted from proton target data. The error bars (bands at the bottom of the panels) represent the statistical (systematic) uncertainties. There is an additional overall 8.6% scale uncertainty arising from the uncertainties in the measurements of the beam and target polarizations. The curves show the results of theoretical calculations using the VGG double-distribution model [47]. The widths of the curves represent the effect of varying the total angular momentum J_u of u-quarks between 0.2 and 0.6, with $J_d = 0$. The bottom row shows the fractional contribution of associated BH production as obtained from a MC simulation. This figure is from ref. [25].

asymmetries A_{LT}^{I} and $A_{LT}^{BH+DVCS}$ are found to be compatible with zero within the total experimental uncertainties. Nevertheless, they may serve as additional constraints in global fits to extract GPDs from measurements. In principle, the asymmetry amplitude $A_{LT,I}^{\sin(\phi-\phi_S)\sin\phi}$ could provide a similar constraint to $\Re e\mathcal{E}$ and to the total angular momentum of quarks [82] through the coefficient $s_{TP_-}^{I}$ (see eq. (50)). However, due to different kinematic prefactors, this amplitude is suppressed compared to those extracted from the single-spin asymmetry A_{UT}^{I}.

The measured asymmetry amplitudes are compatible with the predictions [82] of the only available GPD-based calculation [47] shown in fig. 35. The width of the theoretical curves correspond to variation of the total angular momentum J_u of u-quarks between 0.2 and 0.6, with $J_d = 0$. These model calculations also indicate that the asymmetries are much less sensitive to quark total angular momentum.

8.2 Planned experiment with CLAS12

The detailed understanding of the transverse structure of the nucleon in terms of the spatial and spin distributions of its partons has been recognized as one of the key objectives of the JLab 12 GeV upgrade project. In this perspective, the planned CLAS12 experiment for DVCS on a transversely polarized target was ranked as "high impact" by the PAC of Jefferson Lab. As was shown in eq. (44) and discussed in sect. 8.1, the single-spin asymmetry for proton-DVCS on a transversely polarized target is the most sensitive observable to the elusive GPD E, which,
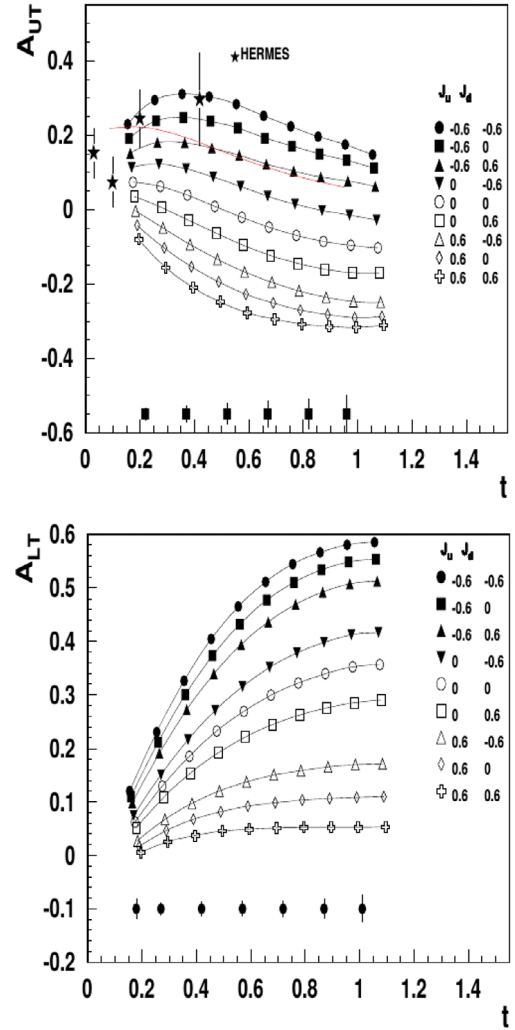
Fig. 36. Expected statistical precision (error bars at the bottom of each plot) for the $\cos\phi$ moment of A_{UT} (top plot) and of the double asymmetry A_{LT} (bottom plot) for the planned CLAS12 experiment of DVCS on transversely polarized target, as a function of $-t$. The symbols joined by curves represent VGG predictions for the two observables, for different combinations of the angular momenta of u and d quarks. The kinematics are $Q^2 = 2.5\,\text{GeV}^2$ and $x_B = 0.2$. Results from HERMES are shown for comparison. The red curve shows the VGG model prediction using the valence approximation for the GPD E. Figures from ref. [83].

along with H, provides access to the quarks' orbital angular momentum via Ji's sum rule (eq. (6)). In particular, the comparison of theory predictions with the HERMES results shown in fig. 34 indicates great sensitivity of the $\cos\phi$ moment of A_{UT} to the contribution of the u quarks to the total angular momentum. Single- and double-spin asymmetry from proton-DVCS on a transversely polarized target will be measured at JLab, with an 11 GeV polarized electron beam and the CLAS12 detector. R&D studies are currently underway for the construction of a transversely polarized HD-Ice target, and alternative target concepts are also being evaluated. The expected pre-

cision of these asymmetries is shown, for one particular kinematic, in fig. 36. In the framework of the VGG model, that parametrizes the GPD E as a function of the quarks' angular momenta, the expected accuracy on the measured observables will allow to discriminate between the possible combinations of J_u and J_d. The measurement will be performed over the same four-dimensional grid of bins as was shown for the CLAS12 BSA, TSA and DSA (sects. 6.4 and 7.3), which will permit to combine these observables for the extraction of all proton CFFs via global or local fitting procedures.

9 DVCS on the neutron

Measuring Deeply Virtual Compton Scattering on a neutron target is one of the necessary steps to complete our understanding of the structure of the nucleon in terms of GPDs. Extracting neutron GPDs is complementary to extracting proton GPDs, as it allows to carry out a quark-flavor separation. In fact,

$$\mathcal{H}^p(\xi,t) = \frac{4}{9}\mathcal{H}^u(\xi,t) + \frac{1}{9}\mathcal{H}^d(\xi,t) \quad (72)$$

and

$$\mathcal{H}^n(\xi,t) = \frac{1}{9}\mathcal{H}^u(\xi,t) + \frac{4}{9}\mathcal{H}^d(\xi,t) \quad (73)$$

(and similarly for E, $\tilde{H}$ and $\tilde{E}$), from which one can obtain

$$\mathcal{H}^u(\xi,t) = \frac{9}{15}(4\mathcal{H}^p(\xi,t) - \mathcal{H}^n(\xi,t)) \quad (74)$$

and

$$\mathcal{H}^d(\xi,t) = \frac{9}{15}(4\mathcal{H}^n(\xi,t) - \mathcal{H}^p(\xi,t)). \quad (75)$$

The importance of neutron targets in the DVCS phenomenology was clearly established in the pioneering Hall A experiment, which has provided, as of today, the only existing data set for neutron DVCS. More data are expected to come from the planned n-DVCS experiments at CLAS12 in the next few years.

9.1 Hall-A n-DVCS experiment

It was shown in eq. (30) that, in the case of DVCS on the neutron, the amplitude of its $\sin\phi$ interference term, that is accessible via helicity-dependent cross section difference or beam-spin asymmetry, is mainly governed by the GPD E, the least known of the GPDs. E is also one of the two GPDs entering Ji's sum rule which links the total angular momentum (J_q) carried by each quark q to the sum of the second moments over x of the GPDs H and E. As was shown in eqs. (74) and (75), in order to make a quark-flavor separation both E^n and E^p are needed. The neutron DVCS channel was explored for the first time in the E03-106 experiment [84] performed in the Hall A of Jefferson Lab. The polarized-beam cross section difference was measured on deuterium and hydrogen targets, and the
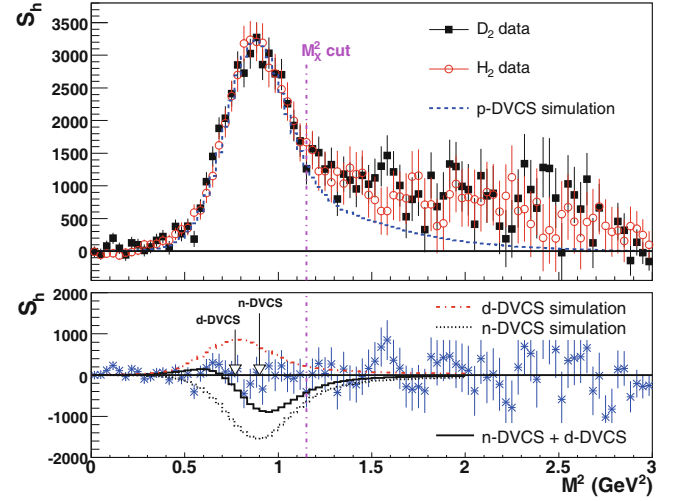
Fig. 37. n-DVCS analysis results from the Hall A experiment [84]. Top: helicity signal (defined as $S_h = \int_0^\pi (N^+ - N^-)\,\mathrm{d}^5\Phi - \int_\pi^{2\pi}(N^+ - N^-)\mathrm{d}^5\Phi$), for $D(e,e',\gamma)$ and $H(e,e',\gamma)$ events; H_2 data are folded with a momentum distribution of the proton in deuterium and scaled to the D_2 data luminosity; the simulation curve is for the Fermi-broadened $H(e,e',\gamma)p$ reaction. Bottom: residual helicity signal after H_2 subtraction; the arrows indicate the M_X^2 average position of n-DVCS and d-DVCS events for $\langle t \rangle = -0.3\,\mathrm{GeV}^2$; the simulation curves are integrated over the acceptance and obtained for the arbitrary values $\mathrm{Im}[C_n^I]^{exp} = -\mathrm{Im}[C_d^I]^{exp} = -1$, where C_n^I and C_d^I depend on the interference of the BH amplitude with the twist-2 Compton form factors. Figure taken from ref. [84].

neutron DVCS and deuteron DVCS signals were extracted from the comparison of experimental yields within the impulse approximation (fig. 37).

These results were limited by their small kinematical coverage, low statistical precision and high systematic uncertainties mostly coming from the subtraction of hydrogen data from deuterium ones. Nonetheless, they allowed, for the first time, a model-dependent extraction of J_u and J_d (fig. 38).

9.2 CLAS12 n-DVCS experiments

The first neutron-DVCS experiment planned with CLAS12 [85] aims to extract beam-spin asymmetries with high accuracy over a wide phase space range taking data on a liquid deuterium target and ensuring the exclusivity by detecting the three active final-state particles ($en\gamma$). Figure 39 shows the expected kinematical coverage and accuracy for the BSA, which will cover the kinematic ranges $1.5 < Q^2 < 6.5\,\mathrm{GeV}^2$, $0.1 < x_B < 0.6$, $0.1 < -t < 1\,\mathrm{GeV}^2$. The sensitivity of the asymmetry to different values of the GPD E, for one of the many (Q^2, x_B, t) bins for which the ϕ-dependence of the BSA will be extracted, is shown in fig. 40. The size of the error bars will be such to allow one to discriminate, in a model-dependent way, between the different hypotheses for J_u and J_d.

Equivalently to the proton case, neutron CFFs can be extracted by measuring various neutron DVCS ob-
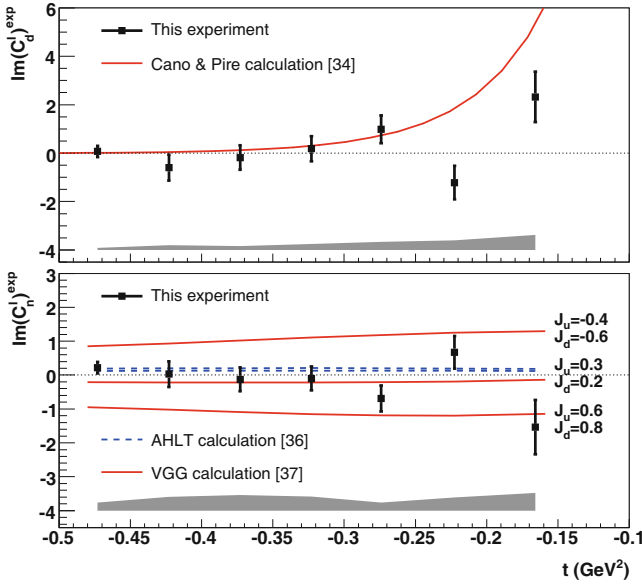
Fig. 38. n-DVCS results from the Hall A experiment [84]: t-dependence of the extracted $\sin(\phi_{\gamma\gamma})$ moments for coherent d-DVCS (top) and incoherent n-DVCS (bottom). Error bars show statistical uncertainties; systematical uncertainties are indicated by the shaded bands. The red curves in the bottom plot show predictions of the VGG model for different values of the quarks' total angular momenta J_u and J_d. This figure is from ref. [84].
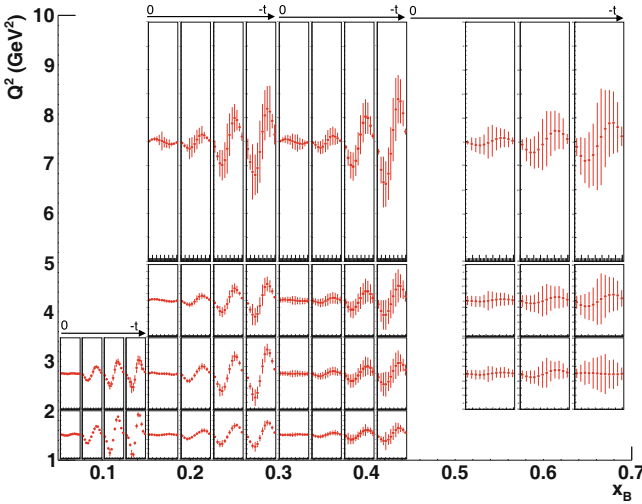
Fig. 39. Expected accuracy, coverage and binning (Q^2, x_B, $-t$, ϕ) for the beam-spin asymmetry for DVCS on the neutron that will be obtained with the planned CLAS12 experiment. The y-scale range, common to all bins, is $(-0.25, 0.25)$. The range in $-t$ is between 0 and $1\,\mathrm{GeV}^2$. Figure from ref. [85].

servables. Therefore, CLAS12 will also perform an experiment of DVCS on the neutron using a longitudinally polarized deuterium target (ND$_3$) [86]. The goal of this experiment is to extract target-spin asymmetries and double-spin asymmetries, similarly to the CLAS E05-114 experiment described in sect. 7.2. These asymmetries, fitted simultaneously with the BSAs that will be
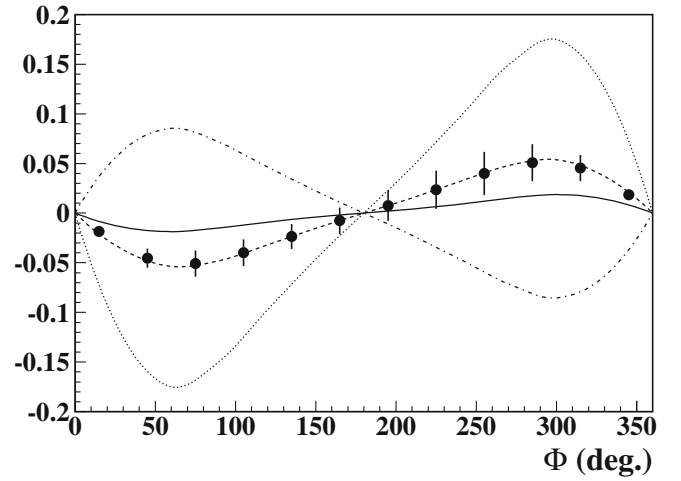
Fig. 40. Projected results for the ϕ-dependence (for $Q^2 = 2.75\,\mathrm{GeV}^2$, $x_B = 0.225$, $-t = 0.35\,\mathrm{GeV}^2$) of the beam-spin asymmetry for DVCS on the neutron with CLAS12. The curves are predictions by the VGG model [28,47] for different values of the quarks' orbital momenta J_u and J_d that, in this model, parametrize the GPD E: $J_u = 0.1$ and $J_d = 0.1$ for the solid line, $J_u = 0.3$ and $J_d = 0.1$ for the dashed line, $J_u = 0.3$ and $J_d = 0.3$ for the dotted line, and $J_u = 0.3$ and $J_d = -0.1$ for the dashed-dotted line. Figure taken from ref. [85].

extracted in the unpolarized neutron-DVCS CLAS12 experiment described beforehand, will allow, for the first time, the model-independent extraction of neutron CFFs. The CFFs which will be obtained with more precision and for most of the kinematic points that will be covered by this experiment are $H_{Im}(n)$ and $E_{Im}(n)$. This is to be expected, since the TSA and the BSA for neutron DVCS are most sensitive to these two CFFs (sect. 2). Combining the obtained neutron CFFs with those that will be extracted from the proton-DVCS measurements will permit, for the first time, a model-independent flavor separation of CFFs.

10 Conclusions and outlook

An overview of all DVCS experiments, either done in the past at HERA (H1 [30–33], ZEUS [35, 38], HERMES [25, 27, 56, 57, 60, 62, 71, 78, 81, 87, 88]) and JLab (6 GeV) (Hall A [36,46,84], CLAS [26,52,53,74,79,80,89]) or impending ones at CERN with COMPASS [37] and with JLab (12 GeV) [49, 50, 70, 83, 85, 90] is provided by fig. 41 in the (Q^2, x_B) kinematic plane, for $1 < Q^2 < 10^3\,\mathrm{GeV}^2$ and $2 \cdot 10^{-5} < x_B < 1$. The complementarity, from the point of view of the covered kinematics, of the experiments performed at HERA (in collider and fixed-target mode) and JLab is evident.

The HERMES Collaboration measured all possible azymuthal asymmetries with respect to charge, beam helicity, and target polarization, for proton DVCS, extracting various ϕ moments. A summary of selected asymmetry amplitudes extracted by HERMES at the average kinematics, using various beam and target configurations for
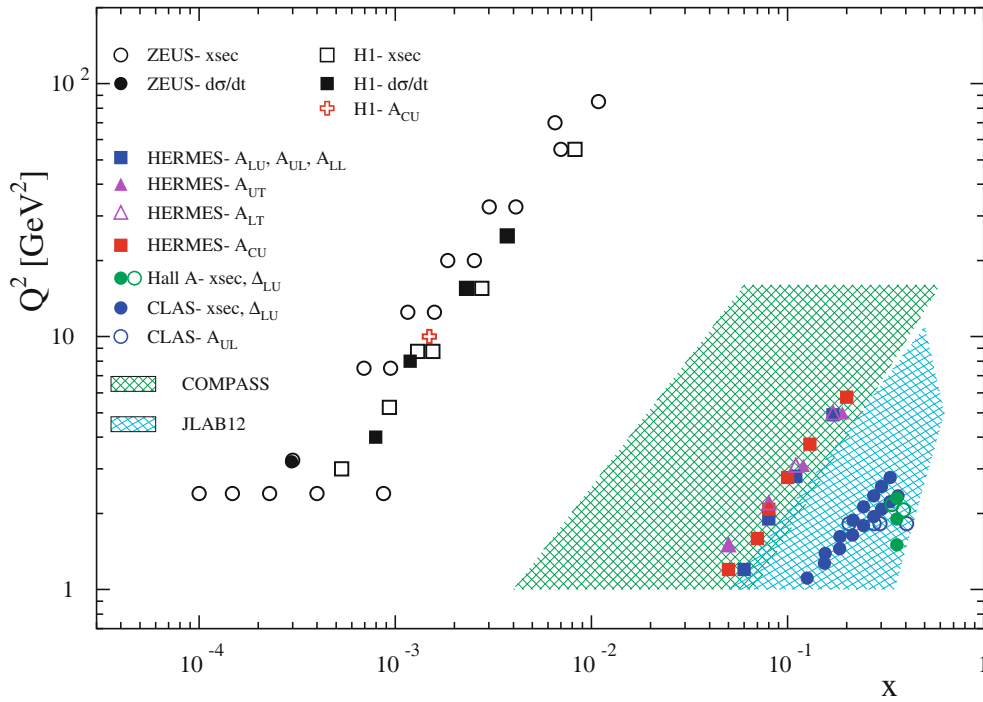
Fig. 41. Overview of all existing and planned measurements of DVCS in the (Q^2, x_B)-plane. The points are measurements done at HERA (H1, ZEUS, HERMES) and JLab (6 GeV). The green and blue domains will be investigated at COMPASS and JLab (12 GeV), respectively, in the next years. Figure taken from ref. [91] and updated by the authors.

hydrogen target is shown in fig. 42. Circles denote the results without the recoil detector. Triangles denote the results obtained detecting the proton in the recoil detector.

In the upper two panels the amplitudes of beam-charge and beam-helicity asymmetries are shown [60, 64, 88]. The significantly different from zero amplitudes $A_C^{\cos(0\phi)}$ and $A_C^{\cos\phi}$ are sensitive to the real part of the CFF $\mathcal{H}$. Measurements with both beam charges and both beam helicities allow to disentangle the two components of the beam-helicity amplitude $A_{LU}^{\sin\phi}$ arising from the interference term and from the DVCS term. The latter, as expected from the HERMES kinematics, is negligible compared to the former. The substantial beam-helicity amplitude $A_{LU,I}^{\sin\phi}$ is of special interest since it is sensitive to the imaginary part of $\mathcal{H}$.

The transverse target single- and double-spin asymmetries [25, 81] are shown in the middle two panels. Here, the amplitude $A_{UT;I}^{\sin(\phi-\phi_s)\cos\phi}$ is significantly different from zero and is of great interest since it gives a rare access to the GPD E.

The amplitudes of the longitudinal target-spin asymmetries [78] are shown in the lower two panels. The A_{UL} amplitudes are sensitive to $\mathrm{Im}(\widetilde{\mathcal{H}})$ and the longitudinal double-spin asymmetries A_{LL} to $\mathrm{Re}(\widetilde{\mathcal{H}})$.

Figure 42 shows also, as a comparison, the results obtained integrating over all the covered kinematics the asymmetries for proton DVCS measured by the CLAS Collaboration (full squares for the E05-114 results, empty square for the E01-113 ones). The CLAS average kinemat-

ics ($\langle Q^2 \rangle = 2.4 \, \mathrm{GeV}^2$, $\langle x \rangle = 0.3$, $\langle -t \rangle = 0.5 \, \mathrm{GeV}^2$) differ from the ones of HERMES mainly for the higher value of x_B. This explains the big difference in the constant term of the double-spin asymmetry: this term, in fact, is dominated by BH, which undergoes strong variations as a function of x_B. It must be pointed out that the measurements carried out at JLab, both in Hall A and CLAS, did not extract ϕ moments like HERMES, but fully differential cross sections and asymmetries, with unpolarized and longitudinally polarized proton target, with high precision and on vast kinematic coverages.

All these amplitudes and ϕ distributions have contributed to the parametrizations of GPD models and for the extraction of GPDs with local and global fits. A partial overview of the current status for the CFFs extraction from the existing proton-DVCS data is provided by fig. 43: here, the $\mathrm{Im}(\mathcal{H})$, $\mathrm{Im}(\widetilde{\mathcal{H}})$, and $\mathrm{Re}(\mathcal{H})$ CFFs, obtained applying the previously described local-fitting procedure [15,55] on Hall-A, CLAS, and HERMES data, are plotted as a function of $-t$. The fit is performed leaving all 8 CFFs as free parameters [92]. For the CLAS case, the example for one (Q^2, x_B) bin, out of the 21 that were fitted, is shown.

The imaginary part of the $\mathcal{H}$ CFF is the term which is best constrained by all existing data. Its real part appears more difficult to determine using the existing absolute DVCS cross sections, while the charge-spin asymmetry seems to be the most powerful tool for this task. It is also evident how the inclusion of longitudinal-target asymmetries is necessary to extract $\mathrm{Im}(\widetilde{\mathcal{H}})$, as well as to reduce the uncertainties on $\mathrm{Im}(\mathcal{H})$.
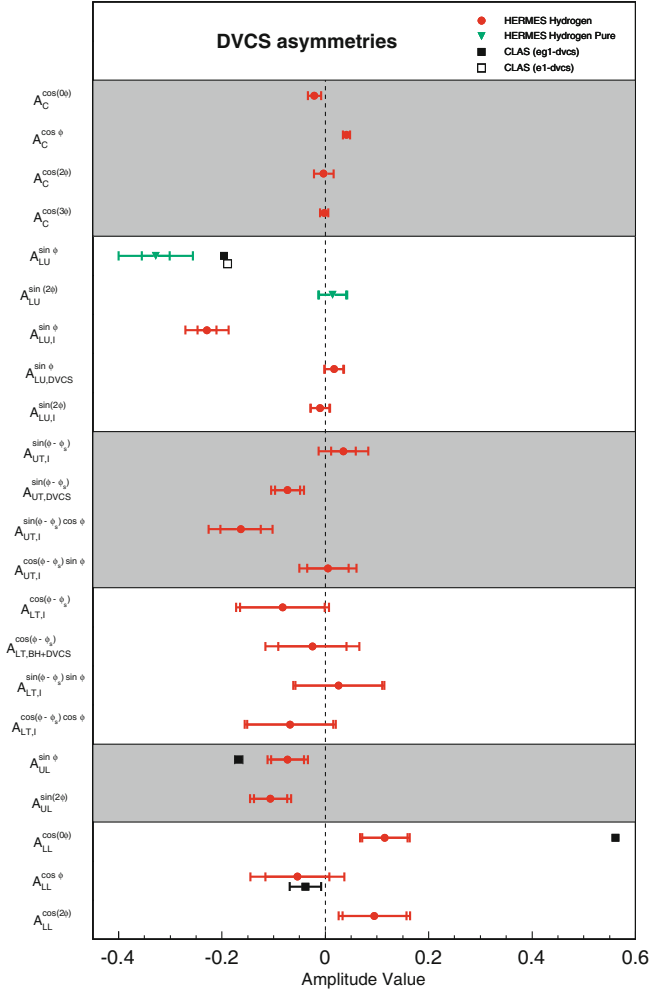
Fig. 42. DVCS overview plot showing selected azimuthal asymmetry amplitudes in the entire HERMES kinematic range (for the average kinematics of each observables, see the corresponding sections) from data collected from 1996 to 2007. This includes data on the unpolarized hydrogen and deuterium targets, the longitudinally polarized hydrogen and deuterium targets and the transversely polarized hydrogen target. Shown are the leading amplitudes of the beam charge, the beam helicity, the target-spin and the double-spin asymmetries. The inner error bars give the statistical uncertainties, the outer error bars the quadratic sum of statistical and systematic uncertainties. The equivalent amplitudes measured by the CLAS Collaboration, integrated over the covered kinematics, are represented by the full squares (E05-114 results) and the empty square (E01-113 result). Figure provided by the HERMES Collaboration and modified by the authors.

Figure 44 shows predictions for the real part (top) and the imaginary part (bottom) of the CFF $\mathcal{H}$ as a function of x_B for two values of t, 0 and $-0.3\,\mathrm{GeV}^2$, according to three different GPD models [93]. It spans over the three orders of magnitude in ξ covered by HERA (in collider mode), COMPASS, HERMES, and JLab. The COMPASS data will bring important information on the exact position of the node for the real part of the CFF. These new results, along with those that will come from the upgraded
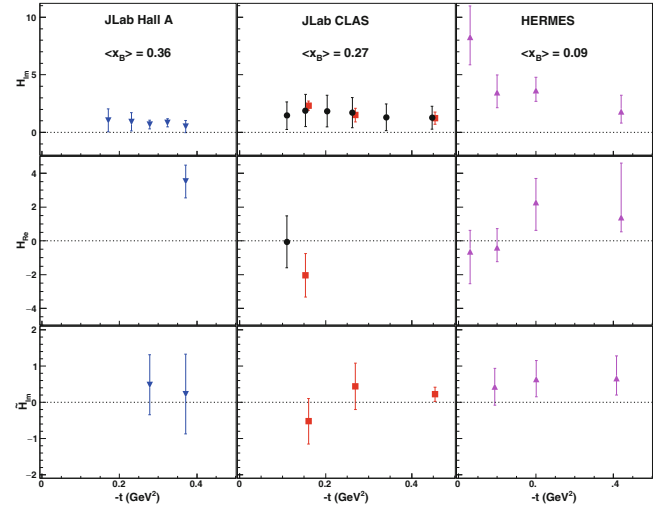

Fig. 43. Proton CFFs, extracted fitting the Hall-A polarized and unpolarized cross sections (first column), the CLAS unpolarized and polarized cross sections alone (second column, black circles) and combined with the polarized target results (TSA and DSA) (second column, red squares) in the second column, and the HERMES results (third column). From top to bottom, H_{Im}, H_{Re}, and $\widetilde{H}_{Im}$ are shown. All 8 CFFs were left as free parameters in the fit. Points courtesy of Michel Guidal.
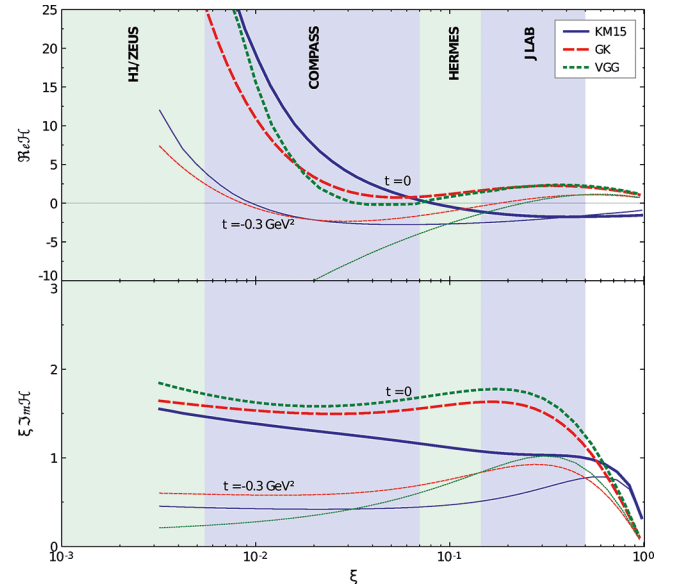
Fig. 44. Real part (top) and imaginary part (bottom) of the CFF $\mathcal{H}$ as a function of x_B for 2 values of $|t|$, computed with the KM15 (blue curves), GK (red curves), and VGG (green curves) models. Figure courtesy of Pawel Sznajder, obtained using the PARTONS platform [93].

JLab, will improve considerably the global determination of GPDs in a large range of ξ from sea quarks to valence quarks, as well as in the gluon sector.
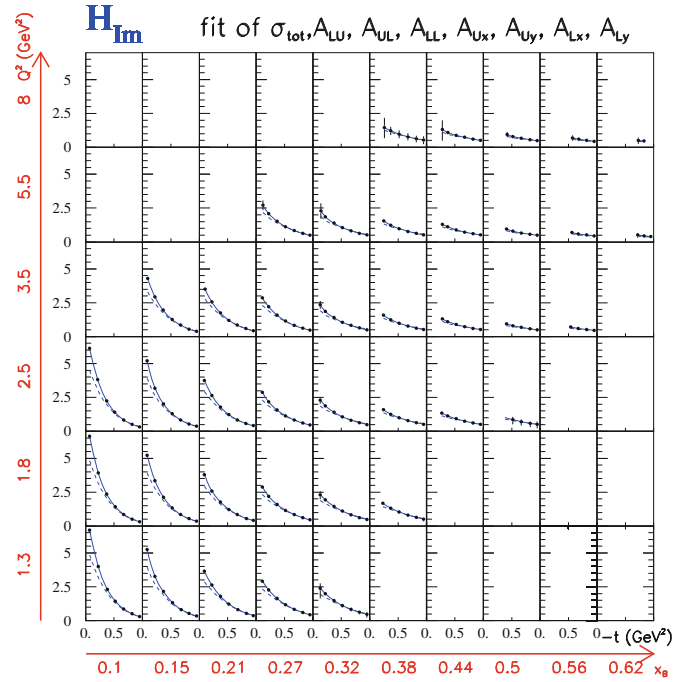
One of the most interesting and challenging purposes of studying GPDs is the possibility of clarifying, via Ji's sum rule, the spin decomposition puzzle. Attempts to extract information on the quark total angular momentum
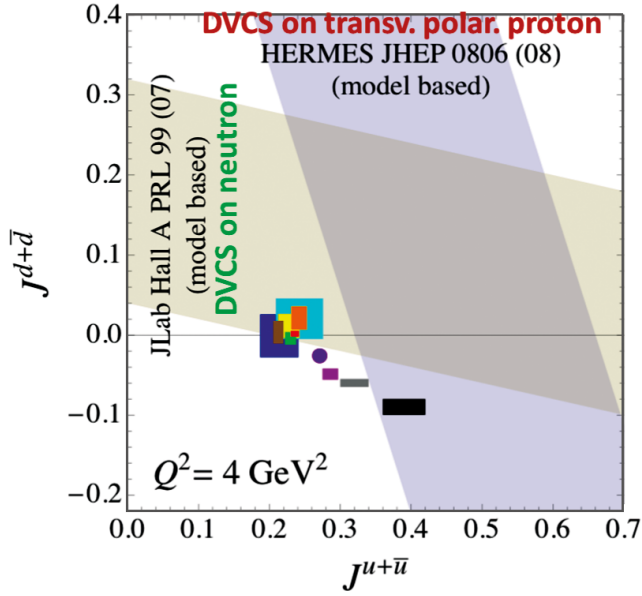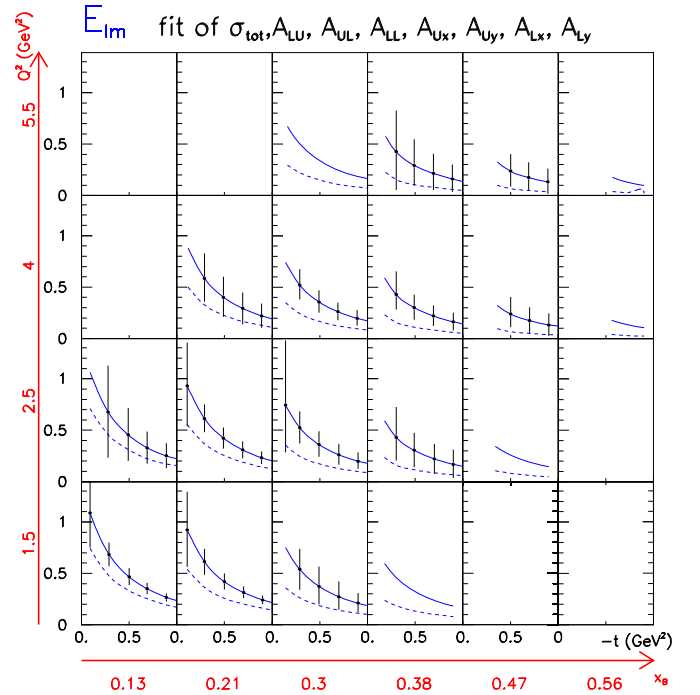
Fig. 45. The data from Hall A for DVCS on the neutron are used to extract, in a model-dependent way, $J_d + J_u/5 = 0.18 \pm 0.14$ [84], while the HERMES results for DVCS on transversely polarized proton yield $J_d + J_u/5 = 0.18 \pm 0.14$ [81]. The VGG model is used for both datasets. Predictions from GPD models (GK [66] (cyan), VGG [11,28,45,47] (brown), Goldstein *et al.* [59] (rose)), form-factors considerations (Diehl *et al.* [44] (violet)), semi-inclusive measurements (Bacchetta and Radici [94]), lattice predictions (LHPC [95] (blue), [96] (red) and QCDSF [97] (green)), quark models (Wakamatsu [98] (yellow) and Thomas [99] (black and grey)).

Fig. 46. The H_{Im} CFF, obtained from the simultaneous fit of the projected results for A_{LU}, A_{UL}, A_{LL}, A_{Ux}, A_{Uy}, A_{Lx}, A_{Ly} and for the unpolarized cross section with the fitting code of refs. [55], is plotted as a function of $-t$ for each Q^2-x_B bin covered by the future CLAS12 proton-DVCS data. The extracted CFFs for which the error bar was larger than 150% were removed. Figure from ref. [15].

have been performed by fitting the parameters J_u and J_d of the VGG model to the DVCS measurements (fig. 45). Although these analyses are very model dependent, the results agree surprisingly well with various models and lattice expectations. The caption of fig. 45 provides the references to such models and lattice calculations.

The experiments planned at JLab at 12 GeV [83,85] will have the ultimate goal to achieve a model-independent measurement of quark-flavor separated CFFs. Figures 46 and 47 show the projected precision and coverage that will be obtained on the proton H_{Im} and E_{Im} CFFs by fitting the proton-DVCS cross section and all the DVCS asymmetries that are planned to be measured with CLAS12. In order to convey the impact of the planned CLAS12 proton- and neutron-DVCS program on our knowledge of GPDs, an example of model-independent flavor separation of CFFs, which the CLAS12 experiments will make possible for the first time, is shown in fig. 48. Here, the CFFs H_{Im} (left) and E_{Im} (right) are shown, as a function of $-t$, for the two nucleons (top, where the proton is represented in black and the neutron in red) and for the two quark flavors (bottom, where black represents u and red d). This figure has been produced using the proton CFFs that were extracted combining all the projected results for the pDVCS asymmetries and cross sections that will be measured with CLAS12 [15], with the neutron CFFs similarly obtained fitting the projected asymmetries for n-DVCS

Fig. 47. Same as caption of fig. 46, but for the E_{Im} CFF. Figure from ref. [15].
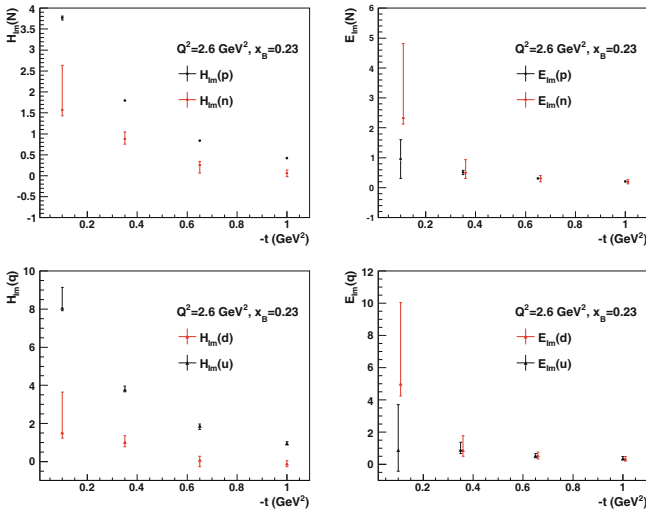
Fig. 48. Top left: $H_{Im}(p)$ (black), extracted from the projections for the approved and conditionally approved proton-DVCS CLAS12 experiments, and $H_{Im}(n)$ (red), obtained from the projections of the approved and conditionally approved neutron-DVCS CLAS12 experiments, as a function of $-t$. Bottom left: Quark-flavor separated H_{Im}, black for u and red for d. The right column shows equivalent results for E_{Im}. Figure taken from ref. [86].

with unpolarized and polarized deuterium target. The flavor separation of the CFFs will represent a major step forward towards the unraveling of the contribution of the quarks' angular momentum to the total nucleon spin via Ji's sum rule.

References

1. M. Diehl, Eur. Phys. J. A **52**, 149 (2016) this Topical Issue, arXiv:1512.01328.
2. D. Mueller, D. Robaschik, B. Geyer, F.M. Dittes, J. Ho.ej.i, Fortsch. Phys. **42**, 101 (1994) hep-ph/9812448.
3. X.-D. Ji, Phys. Rev. Lett. **78**, 610 (1997) hep-ph/9603249.
4. X.-D. Ji, Phys. Rev. D **55**, 7114 (1997) hep-ph/9609381.
5. A.V. Radyushkin, Phys. Lett. B **380**, 417 (1996) hep-ph/9604317.
6. A.V. Radyushkin, Phys. Rev. D **56**, 5524 (1997) hep-ph/9704207.
7. J.C. Collins, L. Frankfurt, M. Strikman, Phys. Rev. D **56**, 2982 (1997) hep-ph/9611433.
8. M. Burkardt, Phys. Rev. D **62**, 071503 (2000) **66**, 119903(E) (2002) hep-ph/0005108.
9. M. Burkardt, Int. J. Mod. Phys. A **18**, 173 (2003) hep-ph/0207047.
10. M. Burkardt, Phys. Lett. B **595**, 245 (2004) hep-ph/0401159.
11. K. Goeke, M.V. Polyakov, M. Vanderhaeghen, Prog. Part. Nucl. Phys. **47**, 401 (2001) hep-ph/0106012.
12. M. Diehl, Phys. Rep. **388**, 41 (2003) hep-ph/0307382.
13. A.V. Belitsky, D. Mueller, A. Kirchner, Nucl. Phys. B **629**, 323 (2002) hep-ph/0112108.
14. A.V. Belitsky, A.V. Radyushkin, Phys. Rep. **418**, 1 (2005) hep-ph/0504030.
15. M. Guidal, H. Moutarde, M. Vanderhaeghen, Rep. Prog. Phys. **76**, 066202 (2013) arXiv:1303.6600.
16. S. Boffi, B. Pasquini, Riv. Nuovo Cimento **30**, 387 (2007) arXiv:0711.2625.
17. L. Favart, M. Guidal, T. Horn, P. Kroll, Eur. Phys. J. A **52**, 158 (2016) this Topical Issue, arXiv:1511.04535.
18. K. Kumericki, S. Liuti, H. Moutarde, Eur. Phys. J. A **52**, 157 (2016) this Topical Issue, arXiv:1602.02763.
19. M. Diehl, private communication.
20. M. Diehl, S. Sapeta, Eur. Phys. J. C **41**, 515 (2005) hep-ph/0503023.
21. A.V. Belitsky, D. Mueller, Phys. Rev. D **79**, 014017 (2009) arXiv:0809.2890.
22. A.V. Belitsky, D. Mueller, Phys. Rev. D **82**, 074010 (2010) arXiv:1005.5209.
23. A.V. Belitsky, D. Müller, Y. Ji, Nucl. Phys. B **878**, 214 (2014) arXiv:1212.6674.
24. A. Bacchetta, U. D'Alesio, M. Diehl, C.A. Miller, Phys. Rev. D **70**, 117504 (2004) hep-ph/0410050.
25. HERMES Collaboration (A. Airapetian *et al.*), Phys. Lett. B **704**, 15 (2011) arXiv:1106.2990.
26. CLAS Collaboration (S. Stepanyan *et al.*), Phys. Rev. Lett. **87**, 182002 (2001) hep-ex/0107043.
27. HERMES Collaboration (A. Airapetian *et al.*), Phys. Rev. Lett. **87**, 182001 (2001) hep-ex/0106068.
28. M. Vanderhaeghen, P.A.M. Guichon, M. Guidal, Phys. Rev. Lett. **80**, 5064 (1998).
29. N. Kivel, M.V. Polyakov, M. Vanderhaeghen, Phys. Rev. D **63**, 114014 (2001) hep-ph/0012136.
30. H1 Collaboration (C. Adloff *et al.*), Phys. Lett. B **517**, 47 (2001) hep-ex/0107005.
31. H1 Collaboration (A. Aktas *et al.*), Eur. Phys. J. C **44**, 1 (2005) hep-ex/0505061.
32. H1 Collaboration (F.D. Aaron *et al.*), Phys. Lett. B **659**, 796 (2008) arXiv:0709.4114.
33. H1 Collaboration (F.D. Aaron *et al.*), Phys. Lett. B **681**, 391 (2009) arXiv:0907.5289.
34. L. Schoeffel, *Deeply virtual Compton scattering at HERA II*, in *Proceedings of the 15th International Workshop on Deep-inelastic scattering and related subjects (DIS 2007), Munich Germany, April 16-20, 2007*, Vols. **1** and **2**, pp. 727–730, arXiv:0705.2925.
35. ZEUS Collaboration (S. Chekanov *et al.*), Phys. Lett. B **573**, 46 (2003) hep-ex/0305028.
36. Jefferson Lab Hall A Collaboration (C.M. Camacho *et al.*), Phys. Rev. Lett. **97**, 262002 (2006) nucl-ex/0607029.
37. COMPASS Collaboration (F. Gautheron *et al.*), COMPASS-II proposal, CERN/SPSC-2010-014, SPSC-P-340 (2010).
38. ZEUS Collaboration (S. Chekanov *et al.*), JHEP **05**, 108 (2009) arXiv:0812.2517.
39. H1 Collaboration (F.D. Aaron *et al.*), JHEP **05**, 032 (2010) arXiv:0910.5831.
40. ZEUS Collaboration (S. Chekanov *et al.*), Nucl. Phys. B **695**, 3 (2004) hep-ex/0404008.
41. A1 Collaboration (J.C. Bernauer *et al.*), Phys. Rev. C **90**, 015206 (2014) arXiv:1307.6227.
42. K. Kumericki, D. Mueller, Nucl. Phys. B **841**, 1 (2010) arXiv:0904.0458.
43. H1 Collaboration (S. Aid *et al.*), Nucl. Phys. B **470**, 3 (1996) hep-ex/9603004.
44. M. Diehl, T. Feldmann, R. Jakob, P. Kroll, Eur. Phys. J. C **39**, 1 (2005) hep-ph/0408173.

45. M. Guidal, M.V. Polyakov, A.V. Radyushkin, M. Vanderhaeghen, Phys. Rev. D **72**, 054013 (2005) hep-ph/0410251.
46. Jefferson Lab Hall A Collaboration (M. Defurne *et al.*), Phys. Rev. C **92**, 055202 (2015) arXiv:1504.05453.
47. M. Vanderhaeghen, P.A.M. Guichon, M. Guidal, Phys. Rev. D **60**, 094017 (1999) hep-ph/9905372.
48. P. Kroll, H. Moutarde, F. Sabatie, Eur. Phys. J. C **73**, 2278 (2013) arXiv:1210.6975.
49. Hall A Collaboration (C. Hyde *et al.*), Jefferson Lab experiment E12-06-114.
50. Hall C Collaboration (C. Munoz *et al.*), Jefferson Lab experiment E12-13-010.
51. CLAS Collaboration (B.A. Mecking *et al.*), Nucl. Instrum. Methods A **503**, 513 (2003).
52. CLAS Collaboration (F.X. Girod *et al.*), Phys. Rev. Lett. **100**, 162002 (2008) arXiv:0711.4805.
53. CLAS Collaboration (H.S. Jo *et al.*), Phys. Rev. Lett. **115**, 212003 (2015) arXiv:1504.02009.
54. K. Kumericki *et al.*, arXiv:1105.0899 (2011).
55. M. Guidal, Eur. Phys. J. A **37**, 319 (2008) **40**, 119(E) (2009) arXiv:0807.2355.
56. HERMES Collaboration (A. Airapetian *et al.*), Phys. Rev. D **75**, 011103 (2007) hep-ex/0605108.
57. HERMES Collaboration (A. Airapetian *et al.*), JHEP **11**, 083 (2009) arXiv:0909.3587.
58. R.J. Barlow, Nucl. Instrum. Methods A **297**, 496 (1990).
59. G.R. Goldstein, J.O. Hernandez, S. Liuti, Phys. Rev. D **84**, 034007 (2011) arXiv:1012.3776.
60. HERMES Collaboration (A. Airapetian *et al.*), JHEP **07**, 032 (2012) arXiv:1203.6287.
61. H. Avakian *et al.*, Nucl. Instrum. Methods A **417**, 69 (1998) hep-ex/9810004.
62. HERMES Collaboration (A. Airapetian *et al.*), JHEP **10**, 042 (2012) arXiv:1206.5683.
63. A. Airapetian *et al.*, JINST **8**, P05012 (2013) arXiv:1302.6092.
64. HERMES Collaboration (A. Airapetian *et al.*), JHEP **01**, 077 (2014) arXiv:1310.5081.
65. J.M. Laget, Phys. Rev. C **76**, 052201 (2007) arXiv:0708.1250.
66. S.V. Goloskokov, P. Kroll, Eur. Phys. J. C **42**, 281 (2005) hep-ph/0501242.
67. S.V. Goloskokov, P. Kroll, Eur. Phys. J. C **53**, 367 (2008) arXiv:0708.3569.
68. S.V. Goloskokov, P. Kroll, Eur. Phys. J. C **65**, 137 (2010) arXiv:0906.0460.
69. K. Kumericki, D. Muller, EPJ Web of Conferences **112**, 01012 (2016) arXiv:1512.09014.
70. CLAS12 Collaboration (F. Sabatie *et al.*), Jefferson Lab experiment E12-06-119.
71. HERMES Collaboration (A. Airapetian *et al.*), Nucl. Phys. B **842**, 265 (2011) arXiv:1008.3996.
72. C.D. Keith *et al.*, Nucl. Instrum. Methods A **501**, 327 (2003).
73. K. Kumercki, D. Muller, M. Murray, Phys. Part. Nucl. **45**, 723 (2014) arXiv:1301.1230.
74. CLAS Collaboration (S. Pisano *et al.*), Phys. Rev. D **91**, 052014 (2015) arXiv:1501.07052.
75. M. Guidal, Phys. Lett. B **689**, 156 (2010) arXiv:1003.0307.
76. A. Bodek, S. Avvakumov, R. Bradford, H.S. Budd, Eur. Phys. J. C **53**, 349 (2008) arXiv:0708.1946.
77. J.O. Gonzalez-Hernandez, S. Liuti, G.R. Goldstein, K. Kathuria, Phys. Rev. C **88**, 065206 (2013) arXiv:1206.1876.
78. HERMES Collaboration (A. Airapetian *et al.*), JHEP **06**, 019 (2010) arXiv:1004.0177.
79. CLAS Collaboration (S. Chen *et al.*), Phys. Rev. Lett. **97**, 072002 (2006) hep-ex/0605012.
80. CLAS Collaboration (E. Seder *et al.*), Phys. Rev. Lett. **114**, 032001 (2015) **114**, 089901 (Addendum) (2015) arXiv:1410.6615.
81. HERMES Collaboration (A. Airapetian *et al.*), JHEP **06**, 066 (2008) arXiv:0802.2499.
82. F. Ellinghaus, W.D. Nowak, A.V. Vinnikov, Z. Ye, Eur. Phys. J. C **46**, 729 (2006) hep-ph/0506264.
83. CLAS12 Collaboration (L. Elouadrhiri *et al.*), Jefferson Lab experiment C12-12-010.
84. Jefferson Lab Hall A Collaboration (M. Mazouz *et al.*), Phys. Rev. Lett. **99**, 242501 (2007) arXiv:0709.0450.
85. CLAS12 Collaboration (S. Niccolai *et al.*), Jefferson Lab experiment E12-11-003.
86. CLAS12 Collaboration (S. Niccolai *et al.*), Jefferson Lab experiment C12-15-004.
87. HERMES Collaboration (A. Airapetian *et al.*), Phys. Rev. C **81**, 035202 (2010) arXiv:0911.0091.
88. HERMES Collaboration (A. Airapetian *et al.*), Nucl. Phys. B **829**, 1 (2010) arXiv:0911.0095.
89. CLAS Collaboration (G. Gavalian *et al.*), Phys. Rev. C **80**, 035206 (2009) arXiv:0812.2950.
90. J. Dudek *et al.*, Eur. Phys. J. A **48**, 187 (2012) arXiv:1208.1244.
91. E.-C. Aschenauer, S. Fazio, K. Kumericki, D. Mueller, JHEP **09**, 093 (2013) arXiv:1304.0077.
92. M. Boër, M. Guidal, J. Phys. G **42**, 034023 (2015) arXiv:1412.4651.
93. B. Berthou *et al.*, arXiv:1512.06174 (2015).
94. A. Bacchetta, M. Radici, Phys. Rev. Lett. **107**, 212001 (2011) arXiv:1107.5755.
95. QCDSF-UKQCD Collaboration (D. Brommel *et al.*), PoS **LAT2007**, 158 (2007) arXiv:0710.1534.
96. UKQCD, QCDSF Collaboration (M. Gockeler *et al.*), Phys. Rev. Lett. **98**, 222001 (2007) hep-lat/0612032.
97. LHPC Collaboration (P. Hagler *et al.*), Phys. Rev. D **77**, 094502 (2008) arXiv:0705.4295.
98. M. Wakamatsu, Eur. Phys. J. A **44**, 297 (2010) arXiv:0908.0972.
99. A.W. Thomas, Phys. Rev. Lett. **101**, 102003 (2008) arXiv:0803.2775.